1 # Temporal and spatial characteristics of ozone depletion

2 # events from measurements in the Arctic

3

4 **J. W. Halfacre[1], T. N. Knepp[1,*], P. B Shepson[1,2], C. R. Thompson[1,**], K. A. Pratt[1,***], B.**

5 **Li[3,****], P. K. Peterson[4], S. J. Walsh[4], W. R. Simpson[4], P. A. Matrai[5], J. W. Bottenheim[6], S.**

6 **Netcheva[7], D. K. Perovich[8], A. Richter[9]**

7 [1]{Department of Chemistry, Purdue University, West Lafayette, Indiana, USA}

8 [2]{Department of Earth, Atmospheric, and Planetary Sciences, Purdue University, West

9 Lafayette, Indiana, USA}

10 [3]{Department of Statistics, Purdue University, West Lafayette, Indiana, USA}

11 [4]{Department of Chemistry, University of Alaska, Fairbanks, Alaska, USA}

12 [5]{Bigelow Laboratory for Ocean Sciences, East Boothbay, Maine, USA}

13 [6]{Air Quality Research Division, Environment Canada, Toronto, Ontario, Canada}

14 [7]{Air Quality Processes Research Section, Environment Canada, Toronto, Ontario, Canada}

15 [8]{U.S. Army Cold Regions Research and Engineering Laboratory, Fairbanks, Alaska, USA}

16 [9]{Institute of Environmental Physics, University of Bremen, Bremen, Germany}

17 [*]{now at Science Systems and Applications, Inc., Hampton, Virginia, USA}

18 [**]{now at Institute of Arctic and Alpine Research, University of Colorado at Boulder, Boulder,

19 Colorado, USA}

20 [***]{now at Department of Chemistry, University of Michigan, Ann Arbor, Michigan, USA}

21 [****]{now at Department of Statistics, University Illinois at Urbana-Champaign, Urbana,

22 Illinois, USA}

23 Correspondence to: J. W. Halfacre (jhalfacr@purdue.edu)

Abstract

Following polar sunrise in the Arctic springtime, tropospheric ozone episodically decreases rapidly to near zero levels during ozone depletion events (ODEs). Many uncertainties remain in our understanding of ODE characteristics, including the temporal and spatial scales, as well as environmental drivers. Measurements of ozone, bromine monoxide (BrO), and meteorology were obtained during several deployments of autonomous, ice-tethered buoys (O-Buoys) from both coastal sites and over the Arctic Ocean; these data were used to characterize observed ODEs. Detected decreases in surface ozone levels during the onset of ODEs corresponded to a median estimated apparent ozone depletion timescale (based on both chemistry and the advection of O_3-depleted air) of 11 hours. If assumed to be dominated by chemical mechanisms, these timescales would correspond to larger-than-observed BrO mole fractions based on known chemistry and assumed other radical levels. Using backward air mass trajectories and an assumption that transport mechanisms dominate observations, the spatial scales for ODEs (defined by time periods in which ozone levels ≤ 15 nmol mol^{-1}) were estimated to be 877 km (median), while areas estimated to represent major ozone depletions (< 10 nmol mol^{-1}) had dimensions of 282 km (median). These observations point to a heterogeneous boundary layer with localized regions of active, ozone-destroying halogen chemistry, interspersed among larger regions of previously depleted air that retain reduced ozone levels through hindered atmospheric mixing. Based on the estimated size distribution, Monte Carlo simulations showed it was statistically possible that all ODEs observed could have originated upwind, followed by transport to the measurement site. Local wind speed averages were low during most ODEs (median of ~3.6 m s^{-1}), and there was no apparent dependence on local temperature.

1 Introduction

Global tropospheric oxidation is generally controlled by ozone (O_3), a major greenhouse gas (Gauss et al., 2006) and the most important precursor to the primary atmospheric oxidant, hydroxyl radical (OH) (Seinfeld and Pandis, 2006; Thompson, 1992). When the sun rises in the Arctic springtime (typically around mid-March), boundary layer O_3 often drops precipitously from background mole fractions of ~40 nmol mol^{-1} (ppbv) to near zero levels for periods of hours, or even days, before recovering (Anlauf et al., 1994; Barrie et al., 1988; Bottenheim et al., 1986; Bottenheim et al., 2002). During these ozone depletion events (ODEs), the prominent regional tropospheric oxidation pathways for hydrocarbons at the surface are driven by species other than OH radicals, notably Cl and Br atoms (Cavender et al., 2008; Jobson et al., 1994).

ODEs are considered to start by the reaction of O_3 with photolytically active halogens, particularly bromine (R1-R2) (Simpson et al., 2007b).

$$Br_2 + h\nu \rightarrow 2Br \tag{R1}$$

$$Br + O_3 \rightarrow BrO + O_2 \tag{R2}$$

O_3 is removed in Reaction (R2) by Br to produce bromine monoxide (BrO). However, BrO is photolabile and can reproduce O_3 and Br in a null cycle. Therefore, the rate at which O_3 is destroyed is ultimately limited by the rate at which BrO reacts with another species to not reform O_3, such as in Reactions (R3-R5).

$$BrO + BrO \rightarrow 2Br + O_2 \tag{R3}$$

$$BrO + ClO \rightarrow BrCl + O_2 \tag{R4a}$$

$$\rightarrow Br + Cl + O_2 \tag{R4b}$$

$$BrO + HO_2 \rightarrow HOBr + O_2 \tag{R5}$$

69　Note that R4 can also produce OClO + Br, but is not listed above as OClO primarily regenerates

70　O_3 in a null cycle via photolysis. Ozone destruction is propagated by the regeneration of reactive

71　halogen species. In the gas phase, Reactions (R3) and (R4) are believed to dominate at high

72　halogen oxide concentrations, while R5 is believed to play a larger role at smaller BrO levels (Le

73　Bras and Platt, 1995; Piot and von Glasow, 2008). Reactions (R3) and (R4) directly reproduce

74　reactive Br atoms, while the HOBr formed by Reaction (R5) must first undergo photolysis

75　(Simpson et al., 2007b, and references therein). Additionally, Reaction (R5) is involved in a

76　series of heterogeneous, autocatalytic reactions referred to as the "bromine explosion", which are

77　believed to supply net atmospheric reactive bromine (Fan and Jacob, 1992; Tang and

78　McConnell, 1996; Vogt et al., 1996; Wennberg, 1999). The "bromine explosion" involves the

79　production of HOBr as above (R5), or through halogen reactions with oxidized nitrogen species

80　(e.g. Aguzzi and Rossi, 2002; Hanson and Ravishankara, 1995). Uptake of this HOBr onto

81　acidic, bromide-containing frozen surfaces produces Br_2 (Adams et al., 2002; Huff and Abbatt,

82　2002), which can then undergo the O_3 destroying reactions once photolyzed (R1). This series of

83　reactions will exponentially increase Br_2 levels until some required reagent runs out.

84　　　Hypothesized sources of reactive halogens include saline frozen surfaces found across the

85　Arctic Ocean, such as the snowpack, blowing snow, and sea salt-derived aerosols (Abbatt et al.,

86　2012; Fan and Jacob, 1992; Frieß et al., 2011; Jones et al., 2009; Simpson et al., 2005; Yang et

87　al., 2008). Recent in situ experiments showed that saline, acidic surface snowpacks (above sea

88　ice or tundra) can act as efficient sources of Br_2, and that the "bromine explosion" can occur

89　within the interstitial air of the snowpack, followed by release of reactive bromine into the

90　boundary layer via wind pumping and diffusion (Pratt et al., 2013).

91   Despite our increasing understanding of the role of halogens in ODEs, basic ODE

92   characteristics, such as their temporal and spatial scales, remain uncertain (Jacobi et al., 2010;

93   Simpson et al., 2007b; Zeng et al., 2003).   Current knowledge of the aforementioned O_3

94   depletion chemical mechanisms (CM) and the corresponding kinetics estimate the timescale for

95   O_3 destruction to be on the order of days (Hausmann and Platt, 1994; Jobson et al., 1994; Piot

96   and von Glasow, 2008, 2009; Tuckermann et al., 1997).   However, there are only a few reports

97   of Arctic ODEs that are assumed/known to have been observed primarily as a result of local

98   scale CM (Boudries and Bottenheim, 2000; Jacobi et al., 2006).   ODEs can also be observed

99   primarily due to air mass transport mechanisms (TM) in which air masses depleted of O_3 (via

100   CM upwind) advect over the measurement site (Morin et al., 2005; Simpson et al., 2007b) and

101   are detected as "ozone depletion events".   Given that the Arctic Ocean surface is sunlit, stable

102   against vertical mixing, and ice-covered during the spring (Lehrer et al., 2004), it has been

103   hypothesized that O_3-depleted surface air could be the norm in the Arctic boundary layer during

104   this time, and that O_3 is only observed at the surface due to turbulent vertical mixing in an

105   otherwise stable boundary layer.   This vertical mixing can temporarily transport free

106   tropospheric O_3 from aloft to the surface, raising the surface level mole fractions to between 30

107   and 40 nmol mol^{-1} (Bottenheim et al., 2009; Hopper et al., 1998; Jacobi et al., 2010; Moore et al.,

108   2014; Strong et al., 2002; Zeng et al., 2003).   Regarding the spatial scales of individual O_3-

109   depleted air masses, Ridley et al. (2003) reported Arctic ODEs extending between 600 and 900

110   km in length from flights during the Tropospheric Ozone Production about the Spring Equinox

111   experiment.   Recently, Jones et al. (2013) reported the observation of multiple ODEs from a

112   network of ten O_3 monitors spread over the Droning Maud Land sector of Antarctica, some of

113   which extended at least 1200 km in horizontal dimension. However, no such network of O_3

114   monitors has yet been established for the Arctic to make analogous observations.

115   In a study of long-term Arctic coastal measurements, Tarasick and Bottenheim (2002)

116   observed that ODEs most often occurred at temperatures of less than 253 K, leading to the

117   proposal that such low temperatures could be necessary for the initiation of ozone depletion.

118   This hypothesis was strengthened by Adams et al. (2002), who reported that frozen NaCl/NaBr

119   surfaces efficiently uptake and react with HOBr to both form and release gas phase Br_2 at

120   temperatures below 253 K. This observation has been hypothesized to occur due to the

121   precipitation of NaCl•$2H_2O$ at temperatures less than 252 K, which then requires a greater

122   concentration of Br^- to maintain the surface brine layer (Cho et al., 2002); when Cl^- precipitates,

123   the volume of the brine water must decrease to maintain the ionic concentration needed for the

124   appropriate freezing point depression. Boundary layer BrO enhancements have been correlated

125   with low temperatures (Nghiem et al., 2012; Zeng et al., 2003), and apparently linear increases in

126   maximum BrO concentrations have been observed with decreasing temperatures, below 258 K

127   (Pöhler et al., 2010). Further, strong positive correlations between O_3 concentration and

128   potential temperature have been reported (Seabrook et al., 2011; Strong et al., 2002). However,

129   Bottenheim et al. (2009) and Neuman et al. (2010) observed ODEs at temperatures as high as

130   267 K, emphasizing uncertainty in the temperatures required for the observation of an O_3-

131   depleted air mass.

132   ODEs have often been associated with a calm, stable boundary layer. Those observed

133   under high wind speeds (faster than 10 m s^{-1}) are generally attributed to TM (Simpson et al.,

134   2007b). Yang et al. (2008) hypothesized that saline snow atop sea ice could disperse during

135   periods of high wind and become a source of both sea-salt aerosol and bromine, consequently

136   initiating ODEs. Indeed, there have been coastal-based studies in which increased BrO and

137   aerosol were observed during periods of elevated wind speeds (> 5 m s^{-1}), and O$_3$ depletion

138   sometimes, but not always, followed (Frieß et al., 2011; Jones et al., 2009). Alternatively, higher

139   wind speeds could also lead to better ventilation of the snowpack in which Br$_2$ is produced

140   (Albert et al., 2002; Foster et al., 2001; Michalowski et al., 2000; Pratt et al., 2013; Toyota et al.,

141   2011). Michalowski et al. (2000) discussed that the rate at which HOBr reacts with Br$^-$ during

142   Br$_2$ production in the "bromine explosion" was dependent on the time scale for turbulent

143   diffusive transport of HOBr to the snowpack surface, which would be wind-speed dependent.

144   However, due to few coincident observations of wind speeds, aerosol, O$_3$, and BrO, the

145   dependence of ODEs on wind speed remains unclear.

146   Arctic air masses depleted in O$_3$ typically spend a significant amount of time over the

147   Arctic Ocean before arriving at coastal measurement sites, suggesting that the ice-covered ocean

148   is the most probable site of ODE initiation (Bottenheim and Chan, 2006; Gilman et al., 2010;

149   Jacobi et al., 2006; Simpson et al., 2007a). In-situ chemical and meteorological data from the

150   Arctic Ocean are, however, sparse. Most long-term Arctic tropospheric O$_3$ measurements have

151   been made at coastal sites, and thus most observed ODEs have been attributed to TM. Attempts

152   to study ODEs over the Arctic Ocean have been conducted on ice floes (e.g., Hopper et al., 1994;

153   Hopper et al., 1998), aircraft (e.g., Jaeschke et al., 1999; Leaitch et al., 1994; Neuman et al.,

154   2010; Ridley et al., 2003; Seabrook et al., 2013; Sheridan et al., 1993), and ships (e.g.,

155   Bottenheim et al., 2009; Gilman et al., 2010; Jacobi et al., 2006; Nghiem et al., 2012; Pöhler et

156   al., 2010; Seabrook et al., 2011). However, few of these studies have produced the long-term

157   data required for in-depth studies of the temporal and spatial scales of ODEs.

158   Recently, a series of ice-tethered buoys were deployed as part of the Arctic Observing

159   Network program to observe ODEs over the Arctic Ocean (Knepp et al., 2010). The buoys have

160   been installed in sea ice for automated, continuous, several-month surface measurements of O_3,

161   BrO (Carlson et al., 2010), carbon dioxide, and local meteorological conditions. The data

162   generated by the O-Buoys represent the first long-term measurements of these chemical species

163   directly over the surface of the ice-covered Arctic Ocean. Using this unique dataset, we estimate

164   the timescales of O_3 depletion, examine the state of our understanding of the chemistry involved,

165   and estimate the spatial extents and meteorological conditions supporting O_3-depleted air masses.

166   **2 Experimental**

167   **2.1 Instrumentation**

168   Surface O_3 and meteorology measurements discussed herein were collected during five

169   separate deployments of O-Buoys (Table 1). Buoy deployment locations are shown in Fig. 1.

170   Details of the O-Buoy design and operation are discussed extensively by Knepp et al. (2010), but

171   a brief description of the meteorological, O_3, and BrO instruments are given herein. At the time

172   of data analysis, BrO data were available from both O-Buoy1 during its 2009 Barrow, AK,

173   deployment, and O-Buoy2 from the Beaufort Sea to compare with O_3 depletion timescales. The

174   O-Buoy2 time series, including O_3, BrO, and temperature, is presented in Fig. 2. During winter

175   months, O-Buoys are set to operate on an abbreviated sampling schedule to conserve power,

176   typically sampling for a total of 4 hours once every 1-3 days. The O-Buoys were switched to 24

177   hour sampling every day close to the time of polar sunrise, typically near the end of February or

178   early March. The MAX-DOAS instrument was an exception to this sampling schedule as it was

179   kept unpowered during the winter months, and turned on during the switch to 24 hour sampling.

180 Though the O-Buoys are also active during fall, winter, and late summer months, we focus

181 mostly on springtime and early summer data herein (dates presented in Table 1).

182   Temperature was measured using a Vaisala model HMP45C temperature and relative

183 humidity probe. Wind speed was measured using a RM Young Model 05103 anemometer. The

184 range of wind speeds observed across the four O-Buoys deployed was 0–15 m s^{-1}. It was

185 observed in the 2009 Barrow, AK, O-Buoy1 deployment, however, that the anemometer was

186 susceptible to icing, which would impede its ability to spin freely and provide accurate

187 measurements. This effect was most prominent during the same deployment, in which wind

188 speed fell from a mean of about 2 m s^{-1} to 0 m s^{-1} for a period of four days. To mitigate the

189 impact of this effect on the interpretation of the results, wind data were not utilized in our

190 analysis when wind speed was measured as 0 m s^{-1}. While there is reason to believe that wind

191 speeds are indeed low during these periods, the actual wind speed is unknown. Thus, if the

192 average wind speed calculated during an ODE contained > 50% of such values, the wind data for

193 that event were not included in the data analysis. We also acknowledge that an icing effect could

194 create a measurement bias toward lower values. However, as discussed in the text (Section 3.3),

195 on average this appears to be a minor issue in terms of our use of the anemometer data (e.g. to

196 calculate ODE spatial scales) as we find effectively equivalent results using our anemometer

197 wind speeds and those estimated using the HYSPLIT backwards trajectory model (Sect. 2.3).

198   Ozone was measured using custom-built 2B Technologies model 205 dual-beam O_3

199 monitors. Customizations include one backup pump, one backup O_3 scrubber, a lamp heater, and

200 modified firmware to control the instrument remotely. The instrument inlet, which contained a

201 90 mm quartz fiber filter (Pall Life Sciences) to prevent intake of large particles, is located on the

202 mast of the buoy ~2 m above the sea ice, while the instrument itself is located inside the hull of

203 the buoy beneath the sea ice such that it operates under a near constant temperature (~ -1.5 °C).

204 The O_3 instrument did not display a temperature-dependence during laboratory, pre-deployment

205 O_3 calibrations as long as the cell temperature of the instrument was stable; cell temperature

206 stabilization generally occurred after 20-30 minutes, and the first 30 minutes of O_3 data during

207 these warm-up periods were excluded from data analysis. The instrument has a manufacturer

208 specified limit of detection of 1 nmol mol^{-1}, and individual measurement uncertainty was

209 calculated to range from 2.1 – 3.5 nmol mol^{-1}. Sample averaging by the ozone monitors differed

210 between buoy deployments: O-Buoy1 used 10 second averages, O-Buoy3 used two second

211 averages, and both O-Buoy2 and O-Buoy 4 used one minute averages. For analysis, all data

212 were smoothed to 5 minute moving averages.

213 BrO was detected using a multi-axis differential optical absorption spectroscopy (MAX-

214 DOAS) instrument. The scan head telescope, located at the top of the buoy mast, collects

215 scattered radiation and sends it through a fiber optic cable to the computer/spectrometer module,

216 which consists of a single board computer (Technologic Systems TS-7260), a stepper motor

217 driver (Stepperboard BC2D15), interface electronics, and a miniature spectrometer (Ocean

218 Optics HR2000, 318-455 nm). The scan elevation angle is controlled by the O-Buoy's

219 supervisory computer and observes light at angles of 90 (zenith), 20, 10, 5, 2, and 1 degree(s)

220 over a period of 30 minutes (Carlson et al., 2010). The zenith spectrum from a 30-minute data

221 measurement period was used as the reference spectrum for the lower elevation angle spectra,

222 which minimizes the differential absorption by stratospheric species. To obtain differential slant

223 column densities (dSCD), the QDOAS software was used (Fayt et al., 2011) to fit both the

224 logarithm of the ratio of each low elevation spectra and zenith spectra in the wavelength region

225 346-364 nm (convolved absorber cross sections detailed in Table 2), as well as a 3rd order

226   polynomial to account for broadband features and a spectral offset to account for stray light. Fit

227   residuals for both O-Buoy1 and O-Buoy2 were less than 1 x 10^{-3} resulting in BrO dSCD errors

228   less than 4 x 10^{13} molecules cm^{-2} and O$_4$ dSCD errors of less than 1x10^{42} molecules^2 cm^{-5}.

229   Retrieval of BrO mole fractions from dSCD data is a two-step inverse problem. First, the aerosol

230   profile is determined from O$_4$ dSCDs using both the SCIATRAN radiative transfer model as a

231   forward model, and the estimation techniques detailed in Frieß et al. (2006). Then, a vertical

232   profile of BrO mole fractions from the ground to 2 km (100 m intervals) was obtained using both

233   the radiative transfer model McArtim (Deutschmann et al., 2011) as a forward model, and

234   similar optimal estimation techniques detailed in Frieß et al. (2011). Because we are only

235   considering surface O$_3$ measurements, only the average BrO mole fractions in the lowest 100 m

236   were used in subsequent portions of this study.

237   The BrO detection limit is a function of the geometry of the observation

238   and the state of the atmosphere at the time of the measurement. We estimated a range for the

239   detection limit (2σ) of 3.7 x 10^{12} (clear sky) to 1.5 x 10^{13} mol cm^{-2} (impaired visibility) for the

240   total integrated column BrO through 2km (VCD$_{2km}$) by looking at the distribution of VCD$_{2km}$

241   values over a month in late summer where no BrO was observed. To evaluate the error

242   associated with the retrieved surface mole fractions, it is necessary to consider both dSCD

243   measurement error and smoothing error (Rodgers, 2000). Smoothing error calculations quantify

244   the error resulting from the inability of the instrument to observe fine structure in the vertical

245   profile. The smoothing error was estimated through considering the mean of an ensemble of

246   profiles retrieved in late summer ($\bar{x}$) when the dSCD measurements indicated no measurable

247   BrO. This allowed us to assume the actual profile (x_a) is given by 0 pmol mol^{-1} (pptv) BrO

248   through 2 km. The average surface mole fraction smoothing errors (ϵ_s) for the entire O-Buoy2

249 campaign were estimated using Eq. 1, where A represents the averaging kernel matrix and I is the

250 identity matrix (Rodgers, 2000).

251 $\epsilon_s = (A - I)(\bar{x} - x_a)$ (1)

252   Individual surface mole fraction errors due to smoothing error averaged 0.3 pmol mol^{-1}

253 for the O-Buoy2 campaign. Including individual mole fraction errors due to propagated dSCD

254 measurement error, total surface mole fraction errors range from 0.7 to 6.9 pmol mol^{-1}, with

255 average and median errors corresponding to ~3.0 and 3.3 pmol mol^{-1} respectively. Due to the

256 timing of the O-Buoy1 deployment, we were unable to estimate smoothing error in the manner

257 described above. Therefore, only errors due to propagated dSCD measurement error were

258 considered. For O-Buoy1, total surface mole fraction errors range from 0.7 to 4.5 pmol mol^{-1},

259 with average and median errors corresponding to ~2.5 and 2.6 pmol mol^{-1} respectively.

260 **2.2 ODE Definition**

261   Ozone depletion events (ODEs) and "major" ozone depletion events (MODEs) are

262 defined when O_3 drops below 15 nmol mol^{-1} and 10 nmol mol^{-1}, respectively, for longer than one

263 hour. The MODE acronym was also utilized by Ridley et al. (2003), and we emphasize that our

264 definition differs from theirs (a larger discussion of ODE definitions in the scientific literature is

265 presented in the Supplement). The ODE start time is the time at which O_3 falls from background

266 (O_3 mole fraction > 25 nmol mol^{-1} for at least 12 hours) to below the 90% value of the mole

267 fraction range during depletion. The ODE stop time is defined by the time when O_3 recovers to

268 90% of the local maximum O_3 mole fraction after rising above 25 nmol mol^{-1} (if background

269 concentrations will ultimately be reestablished). For MODEs, the start time is the time at which

270 O_3 falls below 10 nmol mol^{-1}, and the stop time is the time when O_3 rises above 10 nmol mol^{-1} (if

271 the O_3 mole fraction will stay above 10 nmol mol^{-1} for at least 12 hours). Finally, for the

272   calculation of the O_3 depletion timescale, an O_3 decrease stop time was defined as the time at

273   which O_3 first reached 10% of the O_3 mole fraction range during O_3 depletion. These definitions

274   are illustrated by Fig. 3a, and are further discussed in the Supplement. It should be noted that the

275   increase in O_3 mole fraction on 17 April 2011 seen in Fig. 3 does not recover above 25 nmol

276   mol^{-1} for longer than 12 hours, and its subsequent decrease does not represent a new ODE.

2.3 Air Mass Trajectory Analysis

278   The NOAA HYSPLIT air mass trajectory model (Draxler and Hess, 1997, 1998; Draxler,

279   1999) was utilized to examine backward trajectories during O_3-depleted conditions, as defined in

280   Sect. 2.2. Backward air mass trajectories were calculated starting from a height of 10 m above

281   ground level using the ODE stop time as the start time of the model (note that three events, one

282   from each O-Buoy 2, 3, and 4, did not have well defined ODE stop times, and thus could not

283   undergo this analysis). Isobaric trajectories were chosen because the stable surface air in which

284   the ODEs occur is typically well isolated from the air aloft (Oltmans et al., 2012; Seabrook et al.,

285   2013); as long as O_3 is in ODE conditions, the air is likely to be surface layer air. The trajectory

286   run lengths were defined by the ODE durations (ODE stop time − ODE start time; see

287   Supplemental Information Fig. S1 for the distribution of ODE time lengths), such that the final

288   point of the backward trajectories corresponded to the defined ODE start times. ODE spatial

289   scales were defined as the maximum distance between any two points of the backward air mass

290   trajectory, as this would represent an upper limit to an event's spatial size (illustrated visually in

291   Fig. 4). This analysis was performed for both the broader ODE definition and MODEs. Of the

292   ODE air masses modeled isobarically, all but one remained near the surface (below 200 m above

293   ground level) throughout the course of the trajectory. The outlying ODE air mass, occurring

294   during O-Buoy1 2009 at Barrow, AK, rose above 800 m and likely did not represent surface

295   layer air; this event was therefore excluded from HYSPLIT analyses. For comparison, we also

296   estimated the ODE spatial scales by the same method using isentropic back trajectories (starting

297   height of 10 m above ground level); by determining the distance between the start and end points

298   for each isobaric trajectory; and by using Eq. 2:

299    $D_{ODE} = v_{wind} \times t_{ODE}$ (2)

300   where D_{ODE} is the ODE diameter, v_{wind} is the average local wind speed from the anemometer,

301   and t_{ODE} is the duration of the ODE.

302   The HYSPLIT model was also used to estimate some meteorological parameters at each

303   position along the isobaric backward trajectories. For this analysis, the average and minimum air

304   temperatures along each trajectory were compared with the temperatures recorded by the O-

305   Buoy during each ODE. The path lengths and time lengths of individual trajectories were used

306   to estimate the average wind speeds of the air masses, which were compared with the wind

307   speeds obtained from the O-Buoy anemometer. Wind rose plots were created based on the

308   quadrant in which the air mass trajectory spent the most time during a given ODE (north (315˚-

309   45˚), south (135˚-225˚), east (45˚-135˚), and west (225˚-315˚)). Only four quadrants were used

310   in the wind rose plots because there is a large level of uncertainty associated with using a back

311   trajectory model for this purpose (Kahl, 1993). The angles used were obtained by calculating the

312   bearing between the O-Buoy and each point along each back trajectory for each ODE.

313   **2.4 Monte Carlo Experiment**

314   A Monte Carlo experiment was performed to determine whether it was statistically

315   possible that the observed ODEs resulted primarily from TM, given the estimated size

316   distribution. In the limit of an ODE as large as the Arctic Ocean, the ODE would be observed at

317   the O-Buoy primarily due to local CM. Thus, for some ODE size limit, it is not feasible for all

318   ODE observations to result from TM. For this simulation experiment, we estimated the

319   probability that assumed circular depletion regions overlap with a point of interest (an O-Buoy)

320   when randomly placed about a defined area represented by the ice-covered Arctic Ocean. The

321   diameters of the circles were defined by the ODE size distribution estimated from Beaufort Sea

322   (O-Buoy1 and O-Buoy2) observations (Sect. 2.3); these particular ODEs were chosen for this

323   exercise because of the similar locations and drift trajectories of the buoys, providing the needed

324   statistics for the analysis. Nineteen ODEs were observed between the two deployments (in 2010

325   and 2011), with ODE sizes ranging from 210 - 3532 km (Supplemental Information Fig. S2).

326   The circles, with sizes taken from the observed size distribution, were simultaneously and

327   randomly placed in an area defined by the average sea ice extent of the Arctic Ocean between

328   March 2010 and 2011 (Fig. 5), as reported by the National Snow & Ice Data Center

329   (http://www.nsidc.org/). We note, however, two O-Buoy2 events were excluded from this

330   analysis. The first was removed due to an undefined ODE spatial scale (discussed in Sect. 2.3).

331   The other ODE size excluded (diameter of 3532 km) was estimated to be larger than the defined

332   area. Thus, a total of 17 circles were used in these simulations. The number of circles that

333   overlapped with the location of the buoy (assumed to be 74.75˚ N, 142˚ W, an approximate

334   location of both O-Buoys 1 and 2) was determined for multiple iterations of the experiments.

335   Figure 5 represents one iteration of the experiment, which was repeated 2000 times in order to

336   obtain a statistical distribution of the number of overlaps. Additionally, a sequence of similar

337   Monte Carlo experiments was repeated for individual ODE sizes 1000 times to obtain the

338   probability that each circle size overlaps with the location of the buoy. This simulation

339   experiment was conducted to examine the relationship between ODE size and the probability

340   that the ODE would only be observed due to TM.

3 Results and Discussion

3.1 Ozone Depletion Timescale

For O-Buoys 1–4, a total of 38 ODEs were observed between the months of February and June (see Table 1 for breakdown of each O-Buoy). On the assumption that O_3 decrease is an exponential decay process, and to express the observed depletion time scales in an objective manner, the apparent O_3 depletion timescale (τ_{O_3}) at the beginning of an ODE was estimated as the reciprocal of the slope of $\ln[O_3]$ versus time (during the period ODE start time - O_3 decrease stop time, as discussed in Sect. 2.2; Fig. 3b). This timescale is observed due to a combination of both CM and TM, though the extent to which each factor affects τ_{O_3} is unknown. Because we are analyzing the slopes, this analysis is mostly insensitive to the ODE start / depletion stop times as long as the depletion range of the plot constitutes the majority of the defined timeframe. As seen in Fig. 6a, τ_{O_3} ranged from 30 minutes to longer than 50 hours (maximum of 14 days), with the majority (76%) shorter than 24 hours (median τ_{O_3} of 11 hours). These timescales correspond to O_3 decrease rates ($-\frac{d[O_3]}{dt}$) that range between 0.02 and 30 nmol mol^{-1} hr^{-1} (average and standard deviation: 3.5 ± 5.4 nmol mol^{-1} hr^{-1}). By comparison, Tuckermann et al. (1997) reported O_3 decrease rates ranging from 0.24 to 7 nmol mol^{-1} hr^{-1} from their measurements in Ny-Ålesund, Spitsbergen. Removing coastal site data (O-Buoy1 2009, deployed in Barrow, AK) from the histogram did not significantly alter the τ_{O_3} distribution. For the six ODEs with τ_{O_3} equal to 50 hours or longer, two cases occurred in June after changes in O_3 levels had become much more gradual, relative to the sporadic and episodic nature of the preceding months (Feb. through May). Apart from these two events, which occurred at higher temperatures, there was no clear difference in the local average wind speeds or temperatures that was unique to the remaining four of these six events. However, a likely cause for these extended

16

364 events is poor vertical mixing in the absence of frontal passages. Recent work by Moore et al.

365 (2014) provides evidence of coastal O_3 recovery to background levels when air passes over open

366 leads. This recovery is hypothesized to occur due to increased convective mixing and downward

367 transport of ozone from aloft. Thus, a longer depletion timescale may also imply a large-scale

368 ice-covered surface.

369   If the observed ODEs were indeed dominated by the CM at the location of the O-Buoys

370 (i.e. TM is minimized in the apparent τ_{O_3}), it is surprising that the majority of cases featured

371 such short apparent timescales of O_3-depletion (τ_{O_3}< 12 h). As discussed in Sect. 1, most

372 previous model estimates of O_3-depletion timescales due to chemistry are on the order of days

373 (Hausmann and Platt, 1994; Jobson et al., 1994; Piot and von Glasow, 2008, 2009; Tuckermann

374 et al., 1997). Generally, fast τ_{O_3} observed at coastal sites have been attributed to TM. In these

375 cases, O_3 has been hypothesized to be chemically destroyed upwind (i.e. over the Arctic Ocean),

376 and the apparent τ_{O_3} is a function of both the rate at which the O_3-depleted air mass travels across

377 the measurement site, and the horizontal concentration gradient at the edges of those air masses.

378 For example, Morin et al. (2005) observed O_3 levels to fall from mole fractions of ~30 nmol mol[-]

379 [1] to less than 5 nmol mol^{-1} in around 3 minutes from over the Arctic Ocean, 6 km off the coast of

380 Alert, Canada. However, fast O_3 depletion attributed to local chemistry has been previously

381 reported: using measurements from aboard the icebreaker RV *Polarstern* in the Arctic Ocean,

382 Jacobi et al. (2006) observed a decrease in O_3 from 40 nmol mol^{-1} to < 1 nmol mol^{-1} in less than

383 7 hours.

384   To interpret the results from the O-Buoys, we first explore the extent to which known

385 chemical mechanisms could account for the observed τ_{O_3} values (i.e. the CM dominates while

386 the TM is minimal). Rates of O_3 loss during ODEs have been previously thought to be limited

387   by Reactions (R3-R4) at high BrO levels, estimated by Eq. 3 below (Le Bras and Platt, 1995;

388   Platt and Janssen, 1995).

389    $(-\frac{d[O_3]}{dt}) = 2k_{BrO+BrO}[BrO]^2 + 2k_{BrO+ClO}[BrO][ClO]$ (3)

390   Recently, Liao et al. (2012) and Liao et al. (2014) report that R3 and R4 only account for around

391   40% of the total O_3-depletion chemistry during the 2009 OASIS field campaign. Thompson et

392   al. (2014), using a 0-D model constrained by chemical data collected during the same campaign,

393   found that Br-atom destruction of O_3 has a low homogeneous gas phase radical propagation

394   chain length (close to 1). Because of this small chain length, the dominant source of Br atoms

395   that destroy O_3 appears to be the photolysis of Br_2 and BrCl emitted from the surface or aerosols

396   (Thompson et al., 2014), and thus most of the BrO that is produced terminates via reaction with

397   HO_2 (R5) (or NO_2 for more polluted areas, such as Barrow, AK). Indeed, estimating the rate

398   using Eq. 3 assumes that all Br atoms are produced from Reactions R3 and R4, which is

399   inconsistent with the observed, often large concentrations of Br_2 (Liao et al., 2012). The BrO

400   termination pathways would result in more heterogeneous recycling of Br atoms. They then

401   compared $\frac{d[O_3]}{dt}$ as calculated by both Eq. 3 and by the net chemical O_3-destruction rate (Eq. 4).

402    $\left(-\frac{d[O_3]}{dt}\right) = k[Br][O_3] + k[Cl][O_3] + k[O(^1D)][H_2O]$ (4)

403    $+k[OH][O_3] + k[HO_2][O_3] - k[BrO][NO]$

404    $-J[BrO] - k[ClO][NO] - J[ClO]$

405   In calculating $\frac{d[O_3]}{dt}$, a regression between the rates showed that using only Eq. 3 underestimates

406   the net $\frac{d[O_3]}{dt}$ (from Eq. 4) by a factor of 4.1 on average by neglecting other chemical pathways

407   (Thompson et al., 2014). Therefore, we estimate the BrO mole fractions required to cause the

408   observed τ_{O_3} according to Eqs. 5 and 6 below. These equations include the factor of 4.1 that

409 accounts for the production of bromine atoms via Br_2 and $BrCl$ photolysis, two molecular

410 halogens derived from heterogeneous recycling of species such as $HOBr$ and $BrONO_2$ on halide-

411 containing aerosols or the saline snowpack (Abbatt et al., 2012; Simpson et al., 2007b). A

412 constant ClO concentration of 1.7×10^8 molecules cm^{-3} (6 pmol mol^{-1} at 248 K and atmospheric

413 pressure) was assumed based on average concentrations measured during the 2009 OASIS

414 campaign (Stephens, 2012).

415 $\left(-\frac{d[O_3]}{dt}\right) = 4.1 \times (2k_{BrO+BrO}[BrO]^2 + 2k_{BrO+ClO}[BrO][ClO])$ (5)

416 $\tau_{O_3} = \frac{[O_3]_{avg}}{4.1 \times (2k[BrO]^2 + 2k[BrO][ClO])}$ (6)

417 Because Thompson et al. (2014) utilized a temperature of 248 K in their model,

418 consistent with average local temperatures at Arctic coastal sites in the springtime, we also use

419 this temperature for our BrO mole fraction estimations. The rate constants $k_{BrO+BrO} = 3.8 \times 10^{-12}$

420 cm^3 molecules^{-1} s^{-1} and $k_{BrO+ClO} = 8.2 \times 10^{-12}$ cm^3 molecules^{-1} s^{-1} were calculated based on Sander

421 et al. (2011) and Atkinson et al. (2007), respectively. However, it should be noted that the rate

422 constants change by only ~7–8% when calculated at 273K ($k_{BrO+BrO} = 3.5 \times 10^{-12}$ cm^3 molecules^{-1}

423 s^{-1} and $k_{BrO+ClO} = 7.6 \times 10^{-12}$ cm^3 molecules^{-1} s^{-1}). We note that $k_{BrO+ClO}$ includes both R4a and

424 R4b. The calculated BrO mole fractions corresponding to the estimated τ_{O_3} range from ~1 pmol

425 mol^{-1} (τ_{O_3} = 356 hours) to 115 pmol mol^{-1} (τ_{O_3}= 28 minutes), with a median of 16 pmol mol^{-1}

426 (Fig. 6b). The majority of the calculated distribution of BrO required is fairly comparable to

427 previously reported enhanced surface BrO mole fraction ranges, which often peak around 20-40

428 pmol mol^{-1} (Hausmann and Platt, 1994; Hönninger et al., 2004b; Pöhler et al., 2010; Tuckermann

429 et al., 1997). Indeed, 32 out of 38 events were calculated to require less than 40 pmol mol^{-1} of

430 BrO for O_3 depletion. If, however, expected BrO were calculated based on Eq. 6 without the

431 factor of 4.1 (i.e. expected BrO based R3 and R4), this number decreases to 20 out of 38 events.

432   For the O-Buoy1 (Barrow, AK) and O-Buoy2 deployments, MAX-DOAS BrO data are available

433   for comparison with the calculated BrO estimations (Fig 6b, c; Table 3). Though these observed

434   BrO mole fractions exhibit maxima higher than 20 pmol mol^{-1} (ex. Fig. 2), the average BrO mole

435   fractions during periods of O_3 decrease (ODE start time – O_3 decrease stop time; Sect. 2.2) were

436   found to be much less than 20 pmol mol^{-1} (Table 3).

437   The amount of BrO data available was dependent on the length of daylight, as the MAX-

438   DOAS is a passive instrument (Carlson et al., 2010). In the case of O-Buoy1 at Barrow, there

439   were not enough BrO data available for most periods of O_3 decrease to produce solid

440   conclusions. However, observed BrO levels for three events were not inconsistent with the

441   calculated BrO levels required for the observed τ_{O_3} (see Supplemental Information Table S1 and

442   Fig. S3). While these three events do not have enough BrO data to merit an in-depth discussion,

443   they are discussed in more detail in the Supplement. For the remaining O-Buoy1 and all O-

444   Buoy2 cases in which there were enough BrO data to make comparisons, observed BrO levels

445   were found to be lower than the calculated BrO required by Eqs. 5 and 6, even when considering

446   the propagated measurement error (Table 3; described in Sect. 2.1). Indeed, in two of the O-

447   Buoy2 cases, the observed BrO levels are less than a tenth of that required. This result is

448   surprising since the Arctic Ocean is the assumed originating site for ODEs. At least for O-

449   Buoy2, the observed BrO, assumed 6 pmol mol^{-1} ClO, and factor of 4.1 (Thompson et al., 2014)

450   cannot account for the apparent τ_{O_3}.

451   Possible reasons for the observed small τ_{O_3} values can be summarized by the following

452   two hypotheses:

453   1) There are chemical mechanisms for O_3 destruction that are currently not being

454   considered, or other radical levels (e.g. IO, ClO, HO_2) are higher than assumed here.

455   2) Most ODEs chemically initiate upwind of the O-Buoys such that the observed τ_{O_3}

456   largely result from TM, as discussed above.

457 Concerning the first hypothesis, iodine radical chemistry has been observed in Antarctica (Saiz-

458 Lopez et al., 2007) and in the sub-Arctic at Hudson Bay (Mahajan et al., 2010). Models have

459 shown that iodine chemistry has the potential to have a significant impact on O_3 destruction

460 chemistry due to the very fast rate constant for IO reaction with BrO (~32 times faster than

461 Reaction (R3)) (Calvert and Lindberg, 2004; Atkinson et al., 2007). In a photochemical box

462 model, Saiz-Lopez et al. (2007) found the ozone loss rate increased by a factor of 4 when iodine

463 was included with bromine chemistry to destroy ozone (via IO + BrO, $k_{IO + BrO} = 1.2$ x 10^{-10} cm^3

464 molecule^{-1} s^{-1} at 248 K). Though previous studies have indicated the presence of active iodine

465 chemistry through enhanced levels of total iodine (Martinez et al., 1999) and filterable iodine

466 (Barrie et al., 1994; Schall and Heumann, 1993), there are currently no measurements of IO in

467 the high Arctic above long path DOAS limits of detection as low as 0.3 pmol mol^{-1} (Pöhler et al.,

468 2010), nor are there estimates of I_2 mole fractions for the Arctic Ocean region. Thus, this

469 possible mechanism remains speculative. Additionally, the enhanced salinity of first year ice

470 could be a reason for enhanced chlorine radical production as compared to coastal (e.g. Barrow)

471 observations, or snowpack sources of HO_x (HONO (Zhou et al., 2001), HCHO (Sumner and

472 Shepson, 1999; Sumner et al., 2002), or H_2O_2 (Hutterli et al., 2001; Jacobi et al., 2002)) could

473 enhance HO_2 levels and thus reactivity.

474   We can potentially test for O_3-depletion chemistry missing from Eqs. 4-6 by examining

475 the distribution of the ozone tendency, $(\frac{d[O_3]}{dt})$, with and without the calculated component from

476 the chemistry included in Eq. 5. First, the observed short-term ozone tendency was calculated

477 for values of dt between consecutive BrO measurements (currently O-Buoy1 at Barrow, and O-

478   Buoy2 in the Beaufort Sea) and plotted in Fig. 7a and 7b. Both distributions are zero centered

479   (average Barrow: 0.15 nmol mol^{-1} hr^{-1}; average Beaufort: 0.01 nmol mol^{-1} hr^{-1}) with heavy tails

480   on each side. Then, $\frac{d[O_3]}{dt}$ was calculated using Eq. 5, as above (Fig. 7c, d); this represents the

481   component of the observed $\frac{d[O_3]}{dt}$ resulting from O_3 depletion chemistry. By subtracting these

482   two results, we obtain the distribution of ozone tendencies not accounted for by the considered

483   chemical mechanisms (Fig. 7e, f). These two distributions (representing all observations, and

484   those with known chemistry removed) do differ significantly after this subtraction at the 95%

485   confidence level according to the Kolmogorov-Smirnov test (p-value = 4.9 x 10^{-4} and 1.4 x 10^{-6}

486   for the O-Buoy1 and 2 results, respectively). Both distribution averages become more shifted

487   from zero, with an average $\frac{d[O_3]}{dt}$ of -0.43 nmol mol^{-1} hr^{-1} for O-Buoy1, and -0.18 nmol mol^{-1} hr^{-1}

488   for O-Buoy2. However, it can be shown that the overall symmetry does slightly improve after

489   subtraction by calculating skewness (Eq. 7),

490    $$\text{skewness} = \frac{\sum_{i=1}^{N}(x_i - \bar{x})^3}{(N-1)s^3}$$ (7)

491   where N represents the number of measurements and s represents the standard deviation of a

492   sample. Skewness decreases in magnitude from -0.38 to -0.25 for the O-Buoy1 at Barrow case,

493   and from -0.82 to -0.80 in the O-Buoy2 in the Beaufort Sea case. Springtime chemical O_3

494   production in the Arctic boundary layer has been found to be essentially negligible (Helmig et

495   al., 2009; Helmig et al., 2012), and so it is likely the positive portions of these distributions result

496   from air mass transport and vertical mixing. This analysis then produces a result not inconsistent

497   with the idea that the remainder of the negative $\frac{d[O_3]}{dt}$ represents air mass transport.

498   Hypothesis two, in which the TM dominates the observed τ_{O_3}, is in line with those of

499   many previous studies (e.g., Bottenheim et al., 2009; Hausmann and Platt, 1994; Jacobi et al.,

500   2010; Morin et al., 2005). As discussed in these studies, fast O_3 depletion can often be attributed

501   to changes in air mass flow, and surface O_3 mole fractions can return to background levels upon

502   the passage of low-pressure systems, with associated enhanced vertical mixing. The idea that

503   most of the negative side of the ozone tendency distribution results from transport and not local

504   chemistry is statistically possible only if the average spatial scale of an ODE region is below

505   some critical size (discussed below in Sect. 3.2).

506   **3.2 ODE spatial scales**

507   To estimate the spatial scales of ODEs, we combined O-Buoy observations with

508   backward air mass trajectory analysis (Sect. 2.3). This analysis assumes O_3 depletes within an

509   air mass upwind via CM, and this air mass subsequently roams across the measurement site; the

510   size of this O_3-depleted air mass can be estimated from the length of time O_3 is depleted and the

511   wind speed (i.e., TM dominates the CM at the observation site). We emphasize, however, that

512   the observations likely involve some combination of both TM and in situ CM, given O-Buoy

513   measurements of BrO, which is indicative of active O_3 depletion chemistry. It is of course

514   conceptually possible that other transport scenarios exist; for instance, conditions could exist in

515   some region upwind that result in the continuous depletion of O_3-containing air masses that pass

516   over this region. This depleted air may then pass over the buoy. If the depleted air remains

517   intact, however, the spatial scale calculations would still apply.

518   As shown in Fig. 8, the median of the one-dimensional length for the ODEs was 877 km.

519   While the estimated size distribution of the MODEs ($O_3 < 10$ nmol mol^{-1}) showed no clear mode,

520   it is clear that the distribution contains mostly (relatively) smaller events, with a median size of

521   282 km. The distribution of results is also consistent with observations by Jones et al. (2013)

522   and Ridley et al. (2003), who both reported ODEs of spatial dimensions of at least 1200 km and

523 between 600 and 900 km, respectively. The results presented here strongly suggest that large

524 areas of the Arctic are at least partially depleted during Arctic springtime with local embedded

525 areas that are more depleted. While these isobaric trajectories likely represent the near-surface

526 transport path of depleted air (Seabrook et al., 2013), we also estimated the ODE spatial scales

527 using isentropic back trajectories (starting at 10 m above ground level) and the local wind speeds

528 using the O-Buoy anemometer (Eq. 2). The means for the isobaric- (1013 ± 379 km), isentropic-

529 (1260 ± 279 km), and local wind speed-based (1154 ± 341 km) spatial scale distributions were

530 statistically similar at the 95% confidence level (confidence intervals reported here).

531 Additionally, spatial scale estimation using the distance between the isobaric trajectory start and

532 end points yielded comparable results (mean 947 ± 238 km).

533   As discussed in Sect. 3.1, known chemical mechanisms with reasonable levels of other

534 radicals could not account for the observed τ_{O_3} values, suggesting these fast τ_{O_3} values were due

535 in large part to TM. A Monte Carlo simulation experiment was conducted with the aim of

536 examining the statistical possibility that all observed ODEs, based on the general ODE definition

537 ($O_3 \leq 15$ nmol mol^{-1}), could have occurred upwind of the buoy and were observed because of

538 TM. As described in Sect. 2.4, the simulations were conducted by randomly placing circles

539 (hypothetical ODEs/source regions) across an area the size of the Arctic Ocean sea ice. These

540 circles were defined using the distribution of ODE spatial scales determined from the 17 events

541 observed by the O-Buoy1 and O-Buoy2 deployments (Fig. S2), which observed O_3-depleted air

542 ~60% of the time between late March and May 2010 and ~65% of the time between mid April

543 and May 2011, respectively. We note that assuming circular regions for ODEs could

544 underestimate the ODE size since it assumes the center of the event passes over the buoy, when

545 in fact a secant is more likely. Additionally, the area could be overestimated if the true ODE

546   shapes are actually elliptical or irregular in shape. For this statistical exercise, we made the

547   assumptions that the circles could appear (initiate) anywhere across the Arctic Ocean, and that

548   the circles could also represent possible sizes of ODE source regions. While there is evidence to

549   suggest the existence of specific source regions favorable to ODE formation (Bottenheim and

550   Chan, 2006; Bottenheim et al., 2009; Koo et al., 2012; Simpson et al., 2007a; Theys et al., 2011),

551   no definitive conclusions have yet been made from in-situ observations regarding either the

552   locations or the sizes of such regions. We also assume that that the circle must be contained

553   wholly within the bounds shown in Fig. 5 in order to equally represent all sizes from the

554   distribution. We acknowledge that this assumption could overestimate the frequency with which

555   ODEs overlap with the buoy, as ODEs have been observed in sub-Arctic regions, such as

556   Kangerlussuaq, Greenland (67˚N, 51˚W; Miller et al., 1997), and Hudson Bay (55˚N, 75˚W;

557   Hönninger et al., 2004a). However, this approach could also underestimate the frequency of

558   overlap, as ODEs that initiate remotely from the buoy would be less likely to be part of the

559   observed distribution of events; in other words, it is also possible that the study region for the

560   Monte Carlo simulation could be too large. It is also assumed that the circles represent fully

561   formed O_3-depleted air masses or source regions, and that a circle overlapping with the buoy

562   represents "local" ODE initiation relative to the O-Buoy.

563   The Monte Carlo simulations show that the randomly placed circles most often do not

564   overlap with the measurement site (Fig. 9a). In fact, only very large sizes (larger than ~1750

565   km) were likely to intercept the O-buoy location with a significant probability (> 10%), as shown

566   in Fig. 9b. Specifically, none of the 17 circles overlapped with the O-Buoy site in 58% of the

567   2000 simulation iterations, and only one circle (in 17) overlapped with the O-Buoy site in 33%

568   of iterations. For the median ODE size, the probability of any individual event overlapping the

569   Buoy was less than 1%, as shown in Fig. 9b. Therefore, the spatial statistics exercise supports

570   the possibility that the overwhelming majority of ODEs observed by the O-Buoys in the Beaufort

571   Sea could have been observed primarily due to TM, and ODEs initiated upwind. We emphasize

572   that this Monte Carlo exercise does not prove that this is the case, only that this hypothesis is not

573   inconsistent with the observed ODE spatial scales. The practical question is then raised as to

574   how many buoys (observation sites) must be present to increase the probability of observing an

575   ODE primarily due to local chemistry (with the assumption of equal probability of initiation

576   across the Arctic Ocean and that ODE sizes represent source regions, as assumed for the Monte

577   Carlo experiment). If, for example, two additional O-Buoys were deployed at the North Pole

578   (86° N, 54° W) and in the East Siberian Sea (75° N, 170° E), both potential sites of future O-

579   Buoy deployments, repeating the simulations showed that five out of 17 circles overlapped with

580   at least one measurement site, with no simulation iterations resulting in zero circle overlaps (Fig.

581   S4). This result emphasizes the need for multiple, simultaneous deployments of O-Buoys across

582   different geographical regions to ensure that local scale chemistry is observed within one

583   deployment season.

584   To examine if there is a consistent upwind region from which ODEs travel, wind rose

585   plots were constructed for the ODEs observed by O-Buoy1 (2010 deployment) and O-Buoy2 in

586   the Beaufort Sea, as shown in Fig. 10. As above, the O-Buoys deployed in the Beaufort Sea

587   were chosen because of their similar locations and drift trajectories, providing the needed

588   statistics for the analysis. During ODEs (Fig. 10a), air masses most commonly traveled from the

589   north (~39% of cases), followed by the east (~33% of cases) and the west (~22% of cases). For

590   the MODE air masses, the trajectories most often originated from the eastern sector (~41% of

591   cases; Fig. 10b), and the northern and western sectors accounted for ~27% of cases each. Finally

592   for cases in which O_3 was not depleted (non-ODE cases; Fig. 10c), the eastern and western

593   sectors each accounted for 35% of cases, and the north accounted for 24%. Only one event in

594   each case showed an air mass originating from the south, toward the Alaskan and Canadian

595   coasts. The results presented are consistent with a hypothesis that all regions that are sea-ice

596   covered can support ODE chemistry. Notably, the region to the east of the buoys (i.e. from the

597   Canadian archipelago and eastern Beaufort Sea) features sea ice that historically contains a high

598   fraction of multi-year ice (Kwok et al., 2009), and GOME satellite imagery has previously

599   shown large amounts of BrO to be present in this region (Choi et al., 2012; Koo et al., 2012;

600   Richter et al., 1998; Salawitch et al., 2010). Using backward air mass trajectories originating

601   from the coastal sites of Alert, Canada, and Zeppelinfjellet, Svalbard, Bottenheim and Chan

602   (2006) suggested that ODE air mass source regions could be in the East Siberian Sea, an area to

603   the northwest of the O-Buoys that features first year ice that breaks up in spring. It should be

604   noted, however, that Bottenheim and Chan (2006) only reported trends during the month of

605   April, as opposed to this study that examined ODEs from as early as February to as late as June

606   (Table 1 and Fig. 2). Unfortunately, there were not enough events per month here to observe any

607   clear monthly source region trends. Additionally, while the ODE and MODE cases show slight

608   preferences for northern or eastern winds, respectively, the non-ODE cases do not appear to

609   differ significantly from the ODE and MODE cases. As recently presented by Moore et al.

610   (2014), it is also possible that O_3 recovers when air passes over open sea ice leads due to

611   convective mixing, and air that passed over unbroken ice was more often O_3-depleted, and thus

612   local sea ice conditions could have a more direct impact on O_3 levels than the wind direction.

613   **3.3 Temperature and wind speed during ODEs**

614   Figure 11 shows the distribution of average temperatures that applied during the ODEs in

615   this study. Local average temperatures during ODEs ranged between 243 K and 273 K (Fig.

616   11a; median 257 K). The apparent mode of the distribution (261 K) is 8 K warmer than the

617   hypothesized required upper limit temperature for rapid ozone depletion (253 K). Indeed, ~66%

618   of the ODEs occurred at average temperatures greater than 253 K. An illustrative event is shown

619   in Fig. 2; the O-Buoy2 ODE occurring in early June shows a noticeable increase in BrO while

620   temperatures average around 270 K. The temperatures for MODEs resulted in a similar

621   distribution (Fig. 11b). If, however, ODEs most often originate upwind from the site of O-

622   Buoys, the local temperatures could be irrelevant, as the actual depletion chemistry may have

623   taken place at a location where the temperature was much lower. To examine this, the isobaric

624   HYSPLIT backward air mass trajectories were utilized to estimate the average temperatures

625   experienced by the observed air mass upwind. In Fig. 11c and 11d, we present histograms of the

626   average temperatures from each air mass trajectory for both ODEs and MODEs, which were

627   observed to be very similar (medians: ~258 K and 257 K for ODE and MODE, respectively) and

628   not significantly different from those measured at the O-Buoys. As with the local observations,

629   ~2/3 of the trajectory temperature averages were above 253 K, though we acknowledge that there

630   is a high level of uncertainty associated with using an air mass back trajectory model for such a

631   purpose in a data sparse region (Kahl, 1993). Additionally, we analyzed the minimum

632   temperatures observed by the O-Buoy and from HYSPLIT trajectories during the same depletion

633   periods. The median minimum temperatures observed at the O-Buoy are 251 K and 253 K for

634   the ODE and MODE cases, respectively. Similarly, the median minimum temperatures obtained

635   from HYSPLIT trajectories are 250 K and 254 K for the ODE and MODE cases, respectively. In

636   both cases, it is interesting that only about half of the events were observed with minimum

637 temperatures less than the eutectic temperature of NaCl (252 K), consistent with the results

638 above. This analysis reveals no apparent temperature dependence for O_3 depletion and shows

639 that temperatures below 253 K were not necessary to observe ozone-depleted air masses,

640 corroborating the conclusions of Bottenheim et al. (2009) and Jacobi et al. (2010).

641   Recent reports discuss the possibility that ODEs can be initiated after blowing snow

642 events (Frieß et al., 2011; Jones et al., 2009; Yang et al., 2008; Yang et al., 2010), which

643 presumably produce the availability of new saline surfaces, whether in suspended aerosol form,

644 or through redeposition of sea salt aerosol to the physical surface. Blowing snow events occur

645 during periods of higher wind speeds (> 8 m s^{-1}) (Frieß et al., 2011), implying that there might be

646 a relationship between wind speed and ODEs. We thus performed an analysis for wind speeds

647 analogous to the temperatures using both local O-Buoy data and HYSPLIT backward

648 trajectories. Figure 12a shows that ODEs observed at the O-Buoy were characterized by low

649 measured wind speeds (median of 3.6 m s^{-1} and a mode of 3.5 m s^{-1}), relative to what is needed

650 for blowing snow. However, there is also a difficulty in this analysis in that, under these

651 circumstances, when the air is most of the time at least partly depleted, such a histogram may

652 reflect, at least in part, the normal distribution of wind speeds found in the Arctic troposphere.

653 Therefore, for comparison, periods when O_3 was not depleted (non-ODEs) were examined (see

654 Supplement). As shown in Fig. S5, there was no apparent difference in the modes for non-ODEs

655 relative to the depleted cases. We reiterate that the O-Buoy wind speed measurements reported

656 here could be biased low (see Sect. 2.1); thus, we compare this distribution to one determined by

657 the HYSPLIT method (described in the Supplement) below.

658   The distribution of average wind speeds along the HYSPLIT trajectories (Fig. 12b)

659 reveals a faster median wind speed of 4.9 m s^{-1}, potentially consistent with ODEs occurring at

660   somewhat higher wind speeds. However, the distribution showed no clear preference for higher

661   wind speeds for ODEs. During non-ODE periods, we found the majority of wind speeds to be

662   between 3 and 6 m s^{-1}, similar to that for the ODE cases (Supplemental Fig. S5b), showing that

663   the wind speeds characterizing the upwind air masses observed for ODEs are not different from

664   those for non-depleted conditions. From this analysis, we found that elevated wind speed

665   appeared to be neither a prerequisite, nor a defining characteristic for ODEs, as also found by

666   Helmig et al. (2012) and Solberg et al. (1996).

4. Conclusions

668   The O-Buoy was developed in part to enable the observation of ODEs at the

669   hypothesized location of their initiation, the frozen Arctic Ocean surface. Surface measurements

670   of ambient O_3, BrO, temperature, and wind speed from five separate O-Buoy deployments were

671   utilized to gain insights into the characteristics of ODEs observed over the Arctic Ocean.

672   The apparent timescales of O_3 depletion during ODEs, based on both CM and TM, were

673   calculated to be shorter (median of 11 hours) than previous modeled chemical estimates (e.g.,

674   Hausmann and Platt, 1994) by a factor of two or more. This observation suggests the O_3

675   depletion timescales are dominated by TM, accelerated chemical mechanisms involving higher

676   radical levels, or novel chemical mechanisms. If TM are assumed to dominate local

677   observations, spatially, the majority of the Arctic Ocean marine boundary layer is likely at least

678   partially depleted in O_3 during spring, suggesting that O_3-depleted air masses remain intact for

679   long periods of time after halogen chemistry has subsided. Regions of MODEs ($O_3 < 10$ nmol

680   mol^{-1}) were, on average, smaller, with a median of 282 km, compared to a median of 877 km for

681   ODEs ($O_3 \leq 15$ nmol mol^{-1}). An expanded network of O_3 monitors across the Arctic Ocean is

682   required to effectively capture the spatial extent of the small, actively O_3-depleting air masses, as

683 well as that of the larger, depleted air masses. Monte Carlo simulations supported the possibility

684 that these spatial ODE sizes are consistent with depletion upwind of the O-Buoy, followed by air

685 mass transport to the buoy. However, the degree to which process dominates local observations

686 of ODEs (TM vs. CM) is unknown, as O-Buoy observations of BrO indicate that there is

687 generally always some degree of chemistry involved. Thus, to further address the question of the

688 O_3 depletion timescales, more long-term O_3 and halogen measurements over the Arctic Ocean

689 sea ice are necessary, particularly in locations such as the East Siberian and Chukchi Seas.

690 There was no apparent temperature dependence observed for the presence of an ODE,

691 and low temperatures (i.e. less than 253 K) were not required for the observation of an ODE.

692 The distribution of wind speeds local to the O-Buoy was moderately low during ODEs (mode of

693 ~3.5 m s^{-1}), showing that ODEs were primarily observed under relatively calm conditions.

694 While higher average wind speeds (median ~5 m s^{-1}) were estimated for the course of the

695 backward air mass trajectory, we did not observe a clear preference for ODEs occurring during

696 higher wind speeds. Concurrent measurements of blowing snow, sea salt aerosol, ozone, and

697 halogens, in addition to wind speed, are required to better understand the relationship between

698 wind speed and ODEs.

699 **Acknowledgements**

714

References

715

716

717 Abbatt, J. P. D., Thomas, J. L., Abrahamsson, K., Boxe, C., Granfors, A., Jones, A. E., King, M.

718 D., Saiz-Lopez, A., Shepson, P. B., Sodeau, J., Toohey, D. W., Toubin, C., von Glasow, R.,

719 Wren, S. N., and Yang, X.: Halogen activation via interactions with environmental ice and snow

720 in the polar lower troposphere and other regions, Atmos. Chem. Phys., 12, 6237-6271,

721 doi:10.5194/Acp-12-6237-2012, 2012.

722 Adams, J. W., Holmes, N. S., and Crowley, J. N.: Uptake and reaction of HOBr on frozen and

723 dry NaCl/NaBr surfaces between 253 and 233 K, Atmos. Chem. Phys., 2, 79-91, 2002.

724 Aguzzi, A., and Rossi, M. J.: Heterogeneous hydrolysis and reaction of $BrONO_2$ and Br_2O on

725 pure ice and ice doped with HBr, J. Phys. Chem. A, 106, 5891-5901, doi:10.1021/Jp014383e,

726 2002.

727 Albert, M. R., Grannas, A. M., Bottenheim, J., Shepson, P. B., and Perron, F. E.: Processes and

728 properties of snow–air transfer in the high Arctic with application to interstitial ozone at Alert,

729 Canada, Atmos. Environ., 36, 2779-2787, doi:10.1016/s1352-2310(02)00118-8, 2002.

730 Anlauf, K. G., Mickle, R. E., and Trivett, N. B. A.: Measurement of Ozone during Polar Sunrise

731 Experiment 1992, J. Geophys. Res., 99, 25345-25353, doi:10.1029/94jd01312, 1994.

732 Atkinson, R., Baulch, D. L., Cox, R. A., Crowley, J. N., Hampson, R. F., Hynes, R. G., Jenkin,

733 M. E., Rossi, M. J., and Troe, J.: Evaluated kinetic and photochemical data for atmospheric

734 chemistry: Volume III - gas phase reactions of inorganic halogens, Atmos. Chem. Phys., 7, 981-

735 1191, doi:10.5194/acp-7-981-2007, 2007.

736 Barrie, L. A., Bottenheim, J. W., Schnell, R. C., Crutzen, P. J., and Rasmussen, R. A.: Ozone

737 Destruction and Photochemical-Reactions at Polar Sunrise in the Lower Arctic Atmosphere,

738 Nature, 334, 138-141, 1988.

739   Barrie, L. A., Staebler, R., Toom, D., Georgi, B., Denhartog, G., Landsberger, S., and Wu, D.:

740   Arctic Aerosol Size-Segregated Chemical Observations in Relation to Ozone Depletion during

741   Polar Sunrise Experiment 1992, J. Geophys. Res., 99, 25439-25451, doi:10.1029/94jd01514,

742   1994.

743   Bottenheim, J. W., Gallant, A. G., and Brice, K. A.: Measurements of NO_y species and O_3 at 82˚

744   N latitude, Geophys. Res. Lett., 13, 113-116, doi:10.1029/GL013i002p00113, 1986.

745   Bottenheim, J. W., Fuentes, J. D., Tarasick, D. W., and Anlauf, K. G.: Ozone in the Arctic lower

746   troposphere during winter and spring 2000 (ALERT2000), Atmos. Environ., 36, 2535-2544,

747   doi:10.1016/s1352-2310(02)00121-8, 2002.

748   Bottenheim, J. W., and Chan, E.: A trajectory study into the origin of spring time Arctic

749   boundary layer ozone depletion, J. Geophys. Res., 111, D19301, doi:10.1029/2006jd007055,

750   2006.

751   Bottenheim, J. W., Netcheva, S., Morin, S., and Nghiem, S. V.: Ozone in the boundary layer air

752   over the Arctic Ocean: measurements during the TARA transpolar drift 2006-2008, Atmos.

753   Chem. Phys., 9, 4545-4557, 2009.

754   Boudries, H., and Bottenheim, J. W.: Cl and Br atom concentrations during a surface boundary

755   layer ozone depletion event in the Canadian high Arctic, Geophys. Res. Lett., 27, 517-520,

756   doi:10.1029/1999gl011025, 2000.

757   Calvert, J. G., and Lindberg, S. E.: Potential influence of iodine-containing compounds on the

758   chemistry of the troposphere in the polar spring. I. Ozone depletion, Atmos. Environ., 38, 5087-

759   5104, doi:10.1016/j.atmosenv.2004.05.049, 2004.

760   Carlson, D., Donohoue, D., Platt, U., and Simpson, W. R.: A low power automated MAX-DOAS

761   instrument for the Arctic and other remote unmanned locations, Atmos. Meas. Tech., 3, 429-439,

762   2010.

763   Cavender, A. E., Biesenthal, T. A., Bottenheim, J. W., and Shepson, P. B.: Volatile organic

764   compound ratios as probes of halogen atom chemistry in the Arctic, Atmos. Chem. Phys., 8,

765   1737-1750, doi:10.5194/acp-8-1737-2008, 2008.

766   Cho, H., Shepson, P. B., Barrie, L. A., Cowin, J. P., and Zaveri, R.: NMR investigation of the

767   quasi-brine layer in ice/brine mixtures, J. Phys. Chem. B, 106, 11226-11232,

768   doi:10.1021/Jp020449+, 2002.

769   Choi, S., Wang, Y., Salawitch, R. J., Canty, T., Joiner, J., Zeng, T., Kurosu, T. P., Chance, K.,

770   Richter, A., Huey, L. G., Liao, J., Neuman, J. A., Nowak, J. B., Dibb, J. E., Weinheimer, A. J.,

771   Diskin, G., Ryerson, T. B., da Silva, A., Curry, J., Kinnison, D., Tilmes, S., and Levelt, P. F.:

772   Analysis of satellite-derived Arctic tropospheric BrO columns in conjunction with aircraft

773   measurements during ARCTAS and ARCPAC, Atmos. Chem. Phys., 12, 1255-1285,

774   doi:10.5194/Acp-12-1255-2012, 2012.

775   Deutschmann, T., Beirle, S., Frieß, U., Grzegorski, M., Kern, C., Kritten, L., Platt, U., Prados-

776   Román, C., Puḳị̄te, J., Wagner, T., Werner, B., and Pfeilsticker, K.: The Monte Carlo

777   atmospheric radiative transfer model McArtim: Introduction and validation of Jacobians and 3D

778   features, J. Quant. Spectrosc. Radiat. Transfer, 112, 1119-1137, 2011.

779   Draxler, R. R., and Hess, G. D.: Description of the HYSPLIT 4 modeling system. NOAA Tech.

780   Memo. ERL ARL-224, NOAA Air Resources Laboratory, Silver Spring, MD, 1997.

781   Draxler, R. R., and Hess, G. D.: An overview of the HYSPLIT 4 modeling system of trajectories,

782   dispersion, and deposition, Aust. Meteor. Mag., 47, 295-308, 1998.

783   Draxler, R. R.: HYSPLIT 4 users's guide, U.S. Dept. of Commerce, National Oceanic and

784   Atmospheric Administration, Environmental Research Laboratories, Air Resources Laboratory,

785   Silver Spring, Md., 1999.

786   Fan, S. M., and Jacob, D. J.: Surface Ozone Depletion in Arctic Spring Sustained by Bromine

787   Reactions on Aerosols, Nature, 359, 522-524, doi:10.1038/359522a0, 1992.

788   Fayt, C., De Smedt, I., Letocart, V., Merlaud, A., Pinardi, G., and Van Roozendael, M.: QDOAS

789   Software User Manual, Belgian Institute for Space Aeronomy, 2011.

790   Foster, K. L., Plastridge, R. A., Bottenheim, J. W., Shepson, P. B., Finlayson-Pitts, B. J., and

791   Spicer, C. W.: The role of Br_2 and BrCl in surface ozone destruction at polar sunrise, Science,

792   291, 471-474, doi:10.1126/science.291.5503.471 2001.

793   Frieß, U., Monks, P. S., Remedios, J. J., Rozanov, A., Sinreich, R., Wagner, T., and Platt, U.:

794   MAX-DOAS O_4 measurements: A new technique to derive information on atmospheric aerosols:

795   2. Modeling studies, J. Geophys. Res., 111, D14203, doi:10.1029/2005JD006618, 2006..

796   Frieß, U., Sihler, H., Sander, R., Pöhler, D., Yilmaz, S., and Platt, U.: The vertical distribution of

797   BrO and aerosols in the Arctic: Measurements by active and passive differential optical

798   absorption spectroscopy, J. Geophys. Res., 116, D00R04, doi:10.1029/2011jd015938, 2011.

799   Gauss, M., Myhre, G., Isaksen, I. S. A., Grewe, V., Pitari, G., Wild, O., Collins, W. J., Dentener,

800   F. J., Ellingsen, K., Gohar, L. K., Hauglustaine, D. A., Iachetti, D., Lamarque, J. F., Mancini, E.,

801   Mickley, L. J., Prather, M. J., Pyle, J. A., Sanderson, M. G., Shine, K. P., Stevenson, D. S., Sudo,

802   K., Szopa, S., and Zeng, G.: Radiative forcing since preindustrial times due to ozone change in

803   the troposphere and the lower stratosphere, Atmos. Chem. Phys., 6, 575-599, 2006.

804   Gilman, J. B., Burkhart, J. F., Lerner, B. M., Williams, E. J., Kuster, W. C., Goldan, P. D.,

805   Murphy, P. C., Warneke, C., Fowler, C., Montzka, S. A., Miller, B. R., Miller, L., Oltmans, S. J.,

806   Ryerson, T. B., Cooper, O. R., Stohl, A., and de Gouw, J. A.: Ozone variability and halogen

807   oxidation within the Arctic and sub-Arctic springtime boundary layer, Atmos. Chem. Phys., 10,

808   10223-10236, 2010.

809   Hanson, D. R., and Ravishankara, A. R.: Heterogeneous Chemistry of Bromine Species in

810   Sulfuric-Acid under Stratospheric Conditions, Geophys. Res. Lett., 22, 385-388,

811   doi:10.1029/94gl03379, 1995.

812   Hausmann, M., and Platt, U.: Spectroscopic measurement of bromine oxide and ozone in the

813   high Arctic during Polar Sunrise Experiment 1992, J. Geophys. Res., 99, 25399-25413,

814   doi:10.1029/94jd01314, 1994.

815   Helmig, D., Cohen, L. D., Bocquet, F., Oltmans, S., Grachev, A., and Neff, W.: Spring and

816   summertime diurnal surface ozone fluxes over the polar snow at Summit, Greenland, Geophys.

817   Res. Lett., 36, L08809, doi:10.1029/2008GL036549, 2009.

818   Helmig, D., Boylan, P., Johnson, B., Oltmans, S., Fairall, C., Staebler, R., Weinheimer, A.,

819   Orlando, J., Knapp, D. J., Montzka, D. D., Flocke, F., Frieß, U., Sihler, H., and Shepson, P. B.:

820   Ozone dynamics and snow-atmosphere exchanges during ozone depletion events at Barrow,

821   Alaska, J. Geophys. Res., 117, D20303, doi:10.1029/2012jd017531, 2012.

822   Hönninger, G., Leser, H., Sebastián, O., and Platt, U.: Ground-based measurements of halogen

823   oxides at the Hudson Bay by active longpath DOAS and passive MAX-DOAS, Geophys. Res.

824   Lett., 31, L04111, doi:10.1029/2003gl018982, 2004a.

825   Hönninger, G., von Friedeburg, C., and Platt, U.: Multi axis differential optical absorption

826   spectroscopy (MAX-DOAS), Atmos. Chem. Phys., 4, 231-254, 2004b.

827 Hopper, J. F., Peters, B., Yokouchi, Y., Niki, H., Jobson, B. T., Shepson, P. B., and Muthuramu,

828 K.: Chemical and Meteorological Observations at Ice Camp Swan during Polar Sunrise

829 Experiment 1992, J. Geophys. Res., 99, 25489-25498, doi:10.1029/94JD02303, 1994.

830 Hopper, J. F., Barrie, L. A., Silis, A., Hart, W., Gallant, A. J., and Dryfhout, H.: Ozone and

831 meteorology during the 1994 Polar Sunrise Experiment, J. Geophys. Res., 103, 1481-1492, 1998.

832 Huff, A. K., and Abbatt, J. P. D.: Kinetics and product yields in the heterogeneous reactions of

833 HOBr with ice surfaces containing NaBr and NaCl, J. Phys. Chem. A, 106, 5279-5287,

834 doi:10.1021/Jp014296m, 2002.

835 Hutterli, M. A., McConnell, J. R., Stewart, R. W., Jacobi, H. W., and Bales, R. C.: Impact of

836 temperature-driven cycling of hydrogen peroxide (H_2O_2) between air and snow on the planetary

837 boundary layer, J. Geophys. Res., 106, 15395-15404, doi:10.1029/2001jd900102, 2001.

838 Jacobi, H. W., Frey, M. M., Hutterli, M. A., Bales, R. C., Schrems, O., Cullen, N. J., Steffen, K.,

839 and Koehler, C.: Measurements of hydrogen peroxide and formaldehyde exchange between the

840 atmosphere and surface snow at Summit, Greenland, Atmos. Environ., 36, 2619-2628,

841 doi:10.1016/S1352-2310(02)00106-1, 2002.

842 Jacobi, H. W., Kaleschke, L., Richter, A., Rozanov, A., and Burrows, J. P.: Observation of a fast

843 ozone loss in the marginal ice zone of the Arctic Ocean, J. Geophys. Res., 111, D15309,

844 doi:10.1029/2005jd006715, 2006.

845 Jacobi, H. W., Morin, S., and Bottenheim, J. W.: Observation of widespread depletion of ozone

846 in the springtime boundary layer of the central Arctic linked to mesoscale synoptic conditions, J.

847 Geophys. Res., 115, D17302, doi:10.1029/2010jd013940, 2010.

848   Jaeschke, W., Salkowski, T., Dierssen, J. P., Trumbach, J. V., Krischke, U., and Günther, A.:

849   Measurements of trace substances in the Arctic troposphere as potential precursors and

850   constituents of Arctic haze, J. Atmos. Chem., 34, 291-319, 1999.

851   Jobson, B. T., Niki, H., Yokouchi, Y., Bottenheim, J., Hopper, F., and Leaitch, R.:

852   Measurements of C_2-C_6 Hydrocarbons during the Polar Sunrise 1992 Experiment - Evidence for

853   Cl atom and Br atom Chemistry, J. Geophys. Res., 99, 25355-25368, doi:10.1029/94JD01243,

854   1994.

855   Jones, A. E., Anderson, P. S., Begoin, M., Brough, N., Hutterli, M. A., Marshall, G. J., Richter,

856   A., Roscoe, H. K., and Wolff, E. W.: BrO, blizzards, and drivers of polar tropospheric ozone

857   depletion events, Atmos. Chem. Phys., 9, 4639-4652, doi:10.5194/Acp-9-4639-2009, 2009.

858   Jones, A. E., Wolff, E. W., Brough, N., Bauguitte, S. J. B., Weller, R., Yela, M., Navarro-

859   Comas, M., Ochoa, H. A., and Theys, N.: The spatial scale of ozone depletion events derived

860   from an autonomous surface ozone network in coastal Antarctica, Atmos. Chem. Phys., 13,

861   1457-1467, doi:10.5194/acp-13-1457-2013, 2013.

862   Kahl, J. D.: A Cautionary Note on the Use of Air Trajectories in Interpreting Atmospheric

863   Chemistry Measurements, Atmos. Environ., Part A, 27, 3037-3038, 1993.

864   Knepp, T. N., Bottenheim, J., Carlsen, M., Carlson, D., Donohoue, D., Friederich, G., Matrai, P.

865   A., Netcheva, S., Perovich, D. K., Santini, R., Shepson, P. B., Simpson, W., Valentic, T.,

866   Williams, C., and Wyss, P. J.: Development of an autonomous sea ice tethered buoy for the study

867   of ocean-atmosphere-sea ice-snow pack interactions: the O-buoy, Atmos. Meas. Tech., 3, 249-

868   261, 2010.

869   Koo, J. H., Wang, Y., Kurosu, T. P., Chance, K., Rozanov, A., Richter, A., Oltmans, S. J.,

870   Thompson, A. M., Hair, J. W., Fenn, M. A., Weinheimer, A. J., Ryerson, T. B., Solberg, S.,

871   Huey, L. G., Liao, J., Dibb, J. E., Neuman, J. A., Nowak, J. B., Pierce, R. B., Natarajan, M., and

872   Al-Saadi, J.: Characteristics of tropospheric ozone depletion events in the Arctic spring: analysis

873   of the ARCTAS, ARCPAC, and ARCIONS measurements and satellite BrO observations,

874   Atmos. Chem. Phys., 12, 9909-9922, doi:10.5194/Acp-12-9909-2012, 2012.

875   Kwok, R., Cunningham, G. F., Wensnahan, M., Rigor, I., Zwally, H. J., and Yi, D.: Thinning and

876   volume loss of the Arctic Ocean sea ice cover: 2003-2008, J. Geophys. Res., 114, C07005,

877   doi:10.1029/2009jc005312, 2009.

878   Le Bras, G., and Platt, U.: A Possible Mechanism for Combined Chlorine and Bromine

879   Catalyzed Destruction of Tropospheric Ozone in the Arctic, Geophys. Res. Lett., 22, 599-602,

880   doi:10.1029/94gl03334, 1995.

881   Leaitch, W. R., Barrie, L. A., Bottenheim, J. W., Li, S. M., Shepson, P. B., Muthuramu, K., and

882   Yokouchi, Y.: Airborne Observations Related to Ozone Depletion at Polar Sunrise, J. Geophys.

883   Res., 99, 25499-25517, 1994.

884   Lehrer, E., Hönninger, G., and Platt, U.: A one dimensional model study of the mechanism of

885   halogen liberation and vertical transport in the polar troposphere, Atmos. Chem. Phys., 4, 2427-

886   2440, 2004.

887   Liao, J., Huey, L. G., Tanner, D. J., Flocke, F. M., Orlando, J. J., Neuman, J. A., Nowak, J. B.,

888   Weinheimer, A. J., Hall, S. R., Smith, J. N., Fried, A., Staebler, R. M., Wang, Y., Koo, J. H.,

889   Cantrell, C. A., Weibring, P., Walega, J., Knapp, D. J., Shepson, P. B., and Stephens, C. R.:

890   Observations of inorganic bromine (HOBr, BrO, and Br_2) speciation at Barrow, Alaska, in spring

891   2009, J. Geophys. Res., 117, D00R16, doi:10.1029/2011jd016641, 2012.

892   Liao, J., Huey, L. G., Liu, Z., Tanner, D. J., Cantrell, C. A., Orlando, J. J., Flocke, F. M.,

893   Shepson, P. B., Weinheimer, A. J., Hall, S. R., Ullmann, K., Beine, H. J., Wang, Y., Ingall, E.

894   D., Stephens, C. R., Hornbrook, R. S., Apel, E. C., Riemer, D., Fried, A., Mauldin Iii, R. L.,

895   Smith, J. N., Staebler, R. M., Neuman, J. A., and Nowak, J. B.: High levels of molecular chlorine

896   in the Arctic atmosphere, Nature Geosci, advance online publication, doi:10.1038/ngeo2046,

897   2014.

898   Mahajan, A. S., Shaw, M., Oetjen, H., Hornsby, K. E., Carpenter, L. J., Kaleschke, L., Tian-

899   Kunze, X., Lee, J. D., Moller, S. J., Edwards, P., Commane, R., Ingham, T., Heard, D. E., and

900   Plane, J. M. C.: Evidence of reactive iodine chemistry in the Arctic boundary layer, J. Geophys.

901   Res., 115, D20303, doi:10.1029/2009jd013665, 2010.

902   Martinez, M., Arnold, T., and Perner, D.: The role of bromine and chlorine chemistry for arctic

903   ozone depletion events in Ny-Ålesund and comparison with model calculations, Ann.

904   Geophysicae, 17, 941-956, doi:10.1007/s00585-999-0941-4, 1999.

905   Michalowski, B. A., Francisco, J. S., Li, S.-M., Barrie, L. A., Bottenheim, J. W., and Shepson, P.

906   B.: A computer model study of multiphase chemistry in the Arctic boundary layer during polar

907   sunrise, J. Geophys. Res., 105, 15131-15145, doi:10.1029/2000jd900004, 2000.

908   Miller, H. L., Weaver, A., Sanders, R. W., Arpag, K., and Solomon, S.: Measurements of arctic

909   sunrise surface ozone depletion events at Kangerlussuaq, Greenland (67°N, 51°W), Tellus B, 49,

910   496-509, doi:10.1034/j.1600-0889.49.issue5.6.x, 1997.

911   Moore, C. W., Obrist, D., Steffen, A., Staebler, R. M., Douglas, T. A., Richter, A., and Nghiem,

912   S. V.: Convective forcing of mercury and ozone in the Arctic boundary layer induced by leads in

913   sea ice, Nature, advance online publication, 10.1038/nature12924, 2014.

914   Morin, S., Hönninger, G. H., Staebler, R. M., and Bottenheim, J. W.: A high time resolution

915   study of boundary layer ozone chemistry and dynamics over the Arctic Ocean near Alert,

916   Nunavut, Geophys. Res. Lett., 32, L08809, doi:10.1029/2004GL022098, 2005.

917   Neuman, J. A., Nowak, J. B., Huey, L. G., Burkholder, J. B., Dibb, J. E., Holloway, J. S., Liao,

918   J., Peischl, J., Roberts, J. M., Ryerson, T. B., Scheuer, E., Stark, H., Stickel, R. E., Tanner, D. J.,

919   and Weinheimer, A.: Bromine measurements in ozone depleted air over the Arctic Ocean,

920   Atmos. Chem. Phys., 10, 6503-6514, doi:10.5194/acp-10-6503-2010, 2010.

921   Nghiem, S. V., Rigor, I. G., Richter, A., Burrows, J. P., Shepson, P. B., Bottenheim, J., Barber,

922   D. G., Steffen, A., Latonas, J., Wang, F. Y., Stern, G., Clemente-Colon, P., Martin, S., Hall, D.

923   K., Kaleschke, L., Tackett, P., Neumann, G., and Asplin, M. G.: Field and satellite observations

924   of the formation and distribution of Arctic atmospheric bromine above a rejuvenated sea ice

925   cover, J. Geophys. Res., 117, D00S05, doi:10.1029/2011JD016268, 2012.

926   Oltmans, S. J., Johnson, B. J., and Harris, J. M.: Springtime boundary layer ozone depletion at

927   Barrow, Alaska: Meteorological influence, year-to-year variation, and long-term change, J.

928   Geophys. Res., 117, D00R18, doi:10.1029/2011JD016889, 2012.

929   Piot, M., and von Glasow, R.: The potential importance of frost flowers, recycling on snow, and

930   open leads for ozone depletion events, Atmos. Chem. Phys., 8, 2437-2467, 2008.

931   Piot, M., and von Glasow, R.: Modelling the multiphase near-surface chemistry related to ozone

932   depletions in polar spring, J. Atmos. Chem., 64, 77-105, doi:10.1007/s10874-010-9170-1, 2009.

933   Pöhler, D., Vogel, L., Frieß, U., and Platt, U.: Observation of halogen species in the Amundsen

934   Gulf, Arctic, by active long-path differential optical absorption spectroscopy, P. Natl. Acad. Sci.,

935   107, 6582-6587, doi:10.1073/pnas.0912231107, 2010.

936   Pratt, K. A., Custard, K. D., Shepson, P. B., Douglas, T. A., Pöhler, D., General, S., Zielcke, J.,

937   Simpson, W. R., Platt, U., Tanner, D. J., Huey, G. L., Carlsen, M., and Stirm, B. H.:

938   Photochemical production of molecular bromine in Arctic surface snowpacks, Nature Geosci, 6,

939   351–356, doi:10.1038/ngeo1779, 2013.

940   Richter, A., Wittrock, F., Eisinger, M., and Burrows, J. P.: GOME observations of tropospheric

941   BrO in northern hemispheric spring and summer 1997, Geophys. Res. Lett., 25, 2683-2686,

942   1998.

943   Ridley, B. A., Atlas, E. L., Montzka, D. D., Browell, E. V., Cantrell, C. A., Blake, D. R., Blake,

944   N. J., Cinquini, L., Coffey, M. T., Emmons, L. K., Cohen, R. C., DeYoung, R. J., Dibb, J. E.,

945   Eisele, F. L., Flocke, F. M., Fried, A., Grahek, F. E., Grant, W. B., Hair, J. W., Hannigan, J. W.,

946   Heikes, B. J., Lefer, B. L., Mauldin, R. L., Moody, J. L., Shetter, R. E., Snow, J. A., Talbot, R.

947   W., Thornton, J. A., Walega, J. G., Weinheimer, A. J., Wert, B. P., and Wimmers, A. J.: Ozone

948   depletion events observed in the high latitude surface layer during the TOPSE aircraft program,

949   J. Geophys. Res., 108, 8356, doi:10.1029/2001jd001507, 2003.

950   Rodgers, C. D.: Inverse Methods for Atmospheric Sounding: Theory and Practice, Series on

951   Atmospheric, Oceanic, and Planetary Physics, edited by: Taylor, F. W., World Scientific

952   Publishing, 2000.

953   Saiz-Lopez, A., Mahajan, A. S., Salmon, R. A., Bauguitte, S. J. B., Jones, A. E., Roscoe, H. K.,

954   and Plane, J. M. C.: Boundary layer halogens in coastal Antarctica, Science, 317, 348-351,

955   doi:10.1126/Science.1141408, 2007.

956   Salawitch, R. J., Canty, T., Kurosu, T., Chance, K., Liang, Q., da Silva, A., Pawson, S., Nielsen,

957   J. E., Rodriguez, J. M., Bhartia, P. K., Liu, X., Huey, L. G., Liao, J., Stickel, R. E., Tanner, D. J.,

958   Dibb, J. E., Simpson, W. R., Donohoue, D., Weinheimer, A., Flocke, F., Knapp, D., Montzka,

959   D., Neuman, J. A., Nowak, J. B., Ryerson, T. B., Oltmans, S., Blake, D. R., Atlas, E. L.,

960   Kinnison, D. E., Tilmes, S., Pan, L. L., Hendrick, F., Van Roozendael, M., Kreher, K., Johnston,

961   P. V., Gao, R. S., Johnson, B., Bui, T. P., Chen, G., Pierce, R. B., Crawford, J. H., and Jacob, D.

962   J.: A new interpretation of total column BrO during Arctic spring, Geophys. Res. Lett., 37,

963   L21805, doi:10.1029/2010GL043798, 2010.

964   Schall, C., and Heumann, K. G.: GC determination of volatile organoiodine and organobromine

965   compounds in Arctic seawater and air samples, Fresenius. J. Anal. Chem., 346, 717-722,

966   doi:10.1007/bf00321279, 1993.

967   Seabrook, J. A., Whiteway, J., Staebler, R. M., Bottenheim, J. W., Komguem, L., Gray, L. H.,

968   Barber, D., and Asplin, M.: LIDAR measurements of Arctic boundary layer ozone depletion

969   events over the frozen Arctic Ocean, J. Geophys. Res., 116, D00S02,

970   doi:10.1029/2011JD016335, 2011.

971   Seabrook, J. A., Whiteway, J. A., Gray, L. H., Staebler, R., and Herber, A.: Airborne lidar

972   measurements of surface ozone depletion over Arctic sea ice, Atmos. Chem. Phys., 13, 6023-

973   6029, doi:10.5194/Acp-13-6023-2013, 2013.

974   Sheridan, P. J., Schnell, R. C., Zoller, W. H., Carlson, N. D., Rasmussen, R. A., Harris, J. M.,

975   and Sievering, H.: Composition of Br-Containing Aerosols and Cases Related to Boundary-

976   Layer Ozone Destruction in the Arctic, Atmos. Environ., Part A, 27, 2839-2849, 1993.

977   Simpson, W. R., Alvarez-Aviles, L., Douglas, T. A., Sturm, M., and Dominé, F.: Halogens in the

978   coastal snow pack near Barrow, Alaska: Evidence for active bromine air-snow chemistry during

979   springtime, Geophys. Res. Lett., 32, L04811, doi:10.1029/2004GL021748, 2005.

980   Simpson, W. R., Carlson, D., Hönninger, G., Douglas, T. A., Sturm, M., Perovich, D., and Platt,

981   U.: First-year sea-ice contact predicts bromine monoxide (BrO) levels at Barrow, Alaska better

982   than potential frost flower contact, Atmos. Chem. Phys., 7, 621-627, 2007a.

983   Simpson, W. R., von Glasow, R., Riedel, K., Anderson, P., Ariya, P., Bottenheim, J., Burrows,

984   J., Carpenter, L. J., Frieß, U., Goodsite, M. E., Heard, D., Hutterli, M., Jacobi, H. W., Kaleschke,

985   L., Neff, B., Plane, J., Platt, U., Richter, A., Roscoe, H., Sander, R., Shepson, P., Sodeau, J.,

986   Steffen, A., Wagner, T., and Wolff, E.: Halogens and their role in polar boundary-layer ozone

987   depletion, Atmos. Chem. Phys., 7, 4375-4418, 2007b.

988   Solberg, S., Schmidbauer, N., Semb, A., Stordal, F., and Hov, O.: Boundary-layer ozone

989   depletion as seen in the Norwegian Arctic in Spring, J. Atmos. Chem., 23, 301-332,

990   doi:10.1007/Bf00055158, 1996.

991   Stephens, C. R.: Studies of tropospheric halogen radical chemistry during ozone and mercury

992   depletion events in the Arctic, Ph.D., Chemistry, Purdue University, West Lafayette, IN, 356 pp.,

993   2012.

994   Thompson, C. R., Shepson, P. B., Liao, J., Huey, L. G., and Cantrell, C.: Bromine atom

995   production and chain propagation during springtime Arctic ozone depletion events in Barrow,

996   Alaska, In preparation, 2014.

997   Strong, C., Fuentes, J. D., Davis, R. E., and Bottenheim, J. W.: Thermodynamic attributes of

998   Arctic boundary layer ozone depletion, Atmos. Environ., 36, 2641-2652, 2002.

999   Sumner, A. L., and Shepson, P. B.: Snowpack production of formaldehyde and its effect on the

1000   Arctic troposphere, Nature, 398, 230-233, 1999.

1001   Sumner, A. L., Shepson, P. B., Grannas, A. M., Bottenheim, J. W., Anlauf, K. G., Worthy, D.,

1002   Schroeder, W. H., Steffen, A., Dominé, F., Perrier, S., and Houdier, S.: Atmospheric chemistry

1003   of formaldehyde in the Arctic troposphere at Polar Sunrise, and the influence of the snowpack,

1004   Atmos. Environ., 36, 2553-2562, doi:10.1016/S1352-2310(02)00105-X, 2002.

1005   Tang, T., and McConnell, J. C.: Autocatalytic release of bromine from Arctic snow pack during

1006   polar sunrise, Geophys. Res. Lett., 23, 2633-2636, doi:10.1029/96gl02572, 1996.

1007   Tarasick, D. W., and Bottenheim, J. W.: Surface ozone depletion episodes in the Arctic and

1008   Antarctic from historical ozonesonde records, Atmos. Chem. Phys., 2, 197-205, 2002.

1009   Theys, N., Van Roozendael, M., Hendrick, F., Yang, X., De Smedt, I., Richter, A., Begoin, M.,

1010   Errera, Q., Johnston, P. V., Kreher, K., and De Mazière, M.: Global observations of tropospheric

1011   BrO columns using GOME-2 satellite data, Atmos. Chem. Phys., 11, 1791-1811,

1012   doi:10.5194/Acp-11-1791-2011, 2011.

1013   Thompson, A. M.: The Oxidizing Capacity of the Earths Atmosphere - Probable Past and Future

1014   Changes, Science, 256, 1157-1165, 1992.

1015   Toyota, K., McConnell, J. C., Lupu, A., Neary, L., McLinden, C. A., Richter, A., Kwok, R.,

1016   Semeniuk, K., Kaminski, J. W., Gong, S.-L., Jarosz, J., Chipperfield, M. P., and Sioris, C. E.:

1017   Analysis of reactive bromine production and ozone depletion in the Arctic boundary layer using

1018   3-D simulations with GEM-AQ: inference from synoptic-scale patterns, Atmos. Chem. Phys.,

1019   11, 3949-3979, 2011.

1020   Tuckermann, M., Ackermann, R., Gölz, C., Lorenzen-Schmidt, H., Senne, T., Stutz, J., Trost, B.,

1021   Unold, W., and Platt, U.: DOAS-observation of halogen radical-catalysed arctic boundary layer

1022   ozone destruction during the ARCTOC-campaigns 1995 and 1996 in Ny-Ålesund, Spitsbergen,

1023   Tellus B, 49, 533-555, 1997.

1024   Vogt, R., Crutzen, P. J., and Sander, R.: A mechanism for halogen release from sea-salt aerosol

1025   in the remote marine boundary layer, Nature, 383, 327-330, 1996.

1026   Wennberg, P.: Atmospheric chemistry - Bromine explosion, Nature, 397, 299-301,

1027   doi:10.1038/16805, 1999.

1028   Yang, X., Pyle, J. A., and Cox, R. A.: Sea salt aerosol production and bromine release: Role of

1029   snow on sea ice, Geophys. Res. Lett., 35, L16815, doi:10.1029/2008gl034536, 2008.

1030   Yang, X., Pyle, J. A., Cox, R. A., Theys, N., and Van Roozendael, M.: Snow-sourced bromine

1031   and its implications for polar tropospheric ozone, Atmos. Chem. Phys., 10, 7763-7773,

1032   doi:10.5194/acp-10-7763-2010, 2010.

1033   Zeng, T., Wang, Y. H., Chance, K., Browell, E. V., Ridley, B. A., and Atlas, E. L.: Widespread

1034   persistent near-surface ozone depletion at northern high latitudes in spring, Geophys. Res. Lett.,

1035   30, 2298, doi:10.1029/2003GL018587, 2003.

1036   Zhou, X. L., Beine, H. J., Honrath, R. E., Fuentes, J. D., Simpson, W., Shepson, P. B., and

1037   Bottenheim, J. W.: Snowpack photochemical production of HONO: a major source of OH in the

1038   Arctic   boundary   layer   in   springtime,   Geophys.   Res.   Lett.,   28,   4087-4090,

1039   doi:10.1029/2001gl013531, 2001.

1040

1041

1042

1043 Table 1: O-Buoy deployment locations and time periods of continuous measurements focused on

1044 herein.

O-Buoy Number	Latitude	Longitude	General Area	Dates of Continuous Measurements	Number of ODEs observed
1	71˚N	156˚W	Barrow, AK	02 Mar 2009 – 19 May 2009	13
1	77˚N	135˚W	Beaufort Sea	22 Mar 2010 – 14 Jul 2010	13
2	74˚N	142˚W	Beaufort Sea	11 Apr 2011 – 22 Jul 2011	6
3	60˚N	90˚W	Hudson Bay	22 Feb 2010 – 27 Mar 2010	3
4	78˚N	112˚W	Borden Island, Nunavut, Canada	04 Apr 2010 – 30 Apr 2010	3

1045

1046

1047   Table 2: Cross sections used in spectral analysis. Each cross section is convolved using an

1048   instrument function determined by the 334 nm Hg peak.

Species	Cross Section Reference
BrO (228 K)	Wilmouth et al. (1999)
O_3 (243 K)	Malicet et al. (1995)
NO_2 (220 K)	Vandaele et al. (1998)
O_4	Hermans et al. (2001)
Ring	Determined from zenith spectra using Chance and Spurr (1997)

1049

1050

1051   Table 3: Average BrO mole fractions during periods of O_3 decrease from O-Buoy2 MAX-

1052   DOAS, the corresponding propagated errors, and the estimated BrO required for the observed O_3

1053   depletion timescales based on Eq. 6 (Sect. 3.1).

ODE start time (UTC)	O_3 decrease stop time (UTC)	Observed τ_{O_3} (hours)	Average observed BrO (pmol mol^{-1})	Measurement uncertainty (pmol mol^{-1})	Estimated BrO required from observed τ_{O_3} (pmol mol^{-1})
15 Apr 2011 18:47	16 Apr 2011 06:41	10.5	7.2	3.5	17.5
19 Apr 2011 04:15	19 Apr 2011 04:53	0.5	5.4	3.5	114.7
26 Apr 2011 14:46	26 Apr 2011 22:29	16.2	5.2	3.2	14.8
03 May 2011 11:37	03 May 2011 14:50	1.6	2.6	2.3	33.5
06 May 2011 12:58	07 May 2011 21:32	11.8	5	3.5	15.1
26 May 2011 21:22	28 May 2011 00:59	40.6	0.9	3.2	9.7

1054

1055

1056
1057 Figure 1: Map of locations at which various O-Buoys (abbreviated OB) were deployed between

1058 2009-2011. For the coordinates, see Table 1. Sea ice extent image is for the month of March

1059 2011. Map courtesy of Google Earth, and sea ice image courtesy of the National Snow and Ice

1060 Data Center.

1061
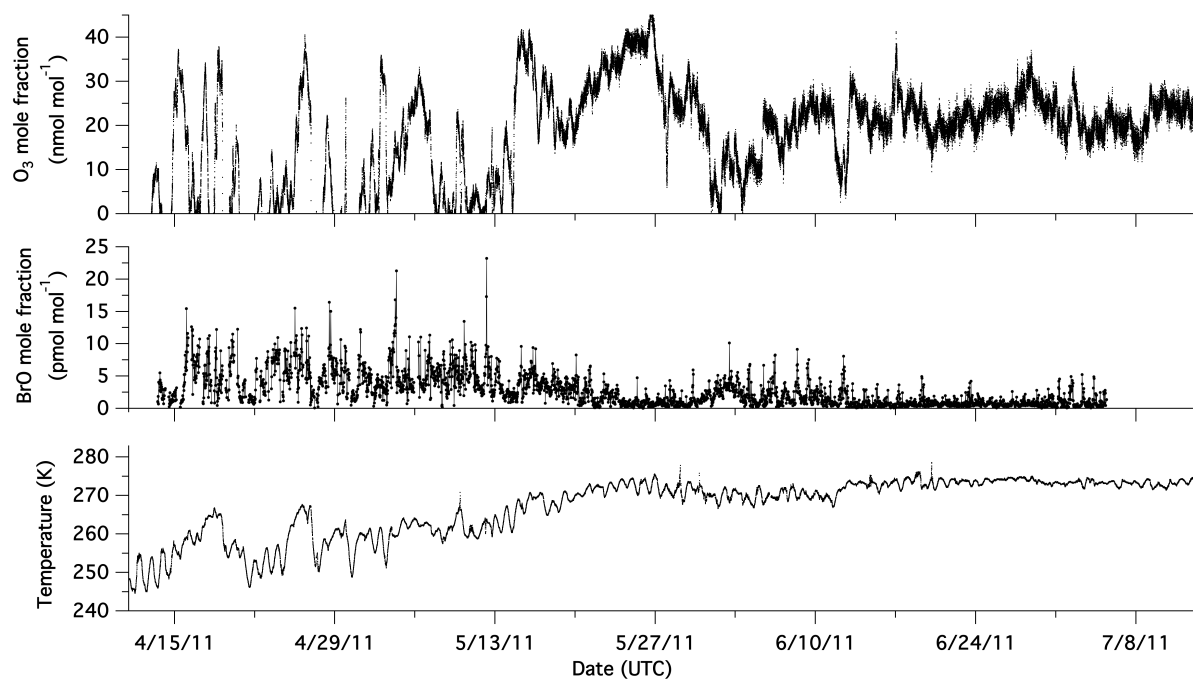
1062   Figure 2: Example time series of O_3, BrO, and temperature from O-Buoy2 during its deployment

1063   in the Beaufort Sea.

1064

1065

1066

1067

1068
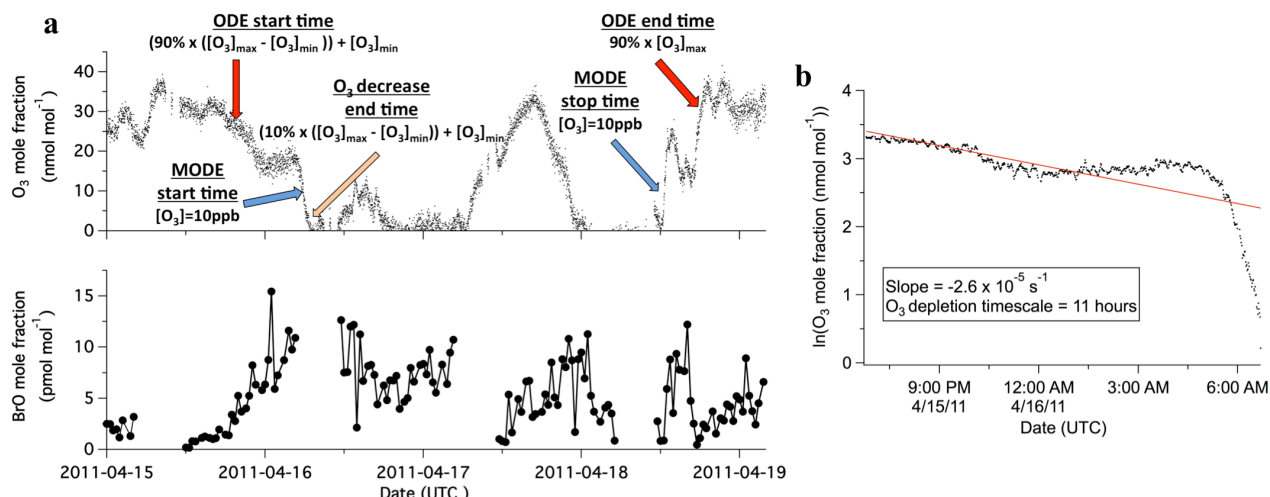
1069

1070 Figure 3: a) Example ODE from O-Buoy2 deployment in the Beaufort Sea with ODE definitions

1071 illustrated. The brief resurgence of O_3 on 17 April does not rise above 25 nmol mol^{-1} for longer

1072 than 12 hours and is thus not considered as separating two ODEs. Error bars are not displayed to

1073 more clearly show the time series. As discussed in Sect. 2.1, individual measurement errors for

1074 O_3 ranged from 2.1 to 3.5 nmol mol^{-1}, and BrO measurement errors ranged from 0.7 to 6.9 pmol

1075 mol^{-1} (median and average error ~3 pmol mol^{-1}). b) Example of O_3 depletion timescale

1076 calculation based on the depletion range (ODE start time – O_3 decrease end time) from a). The

1077 natural logarithm of the O_3 values is plotted against time, and the inverse slope of this plot

1078 represents the O_3 depletion timescale.
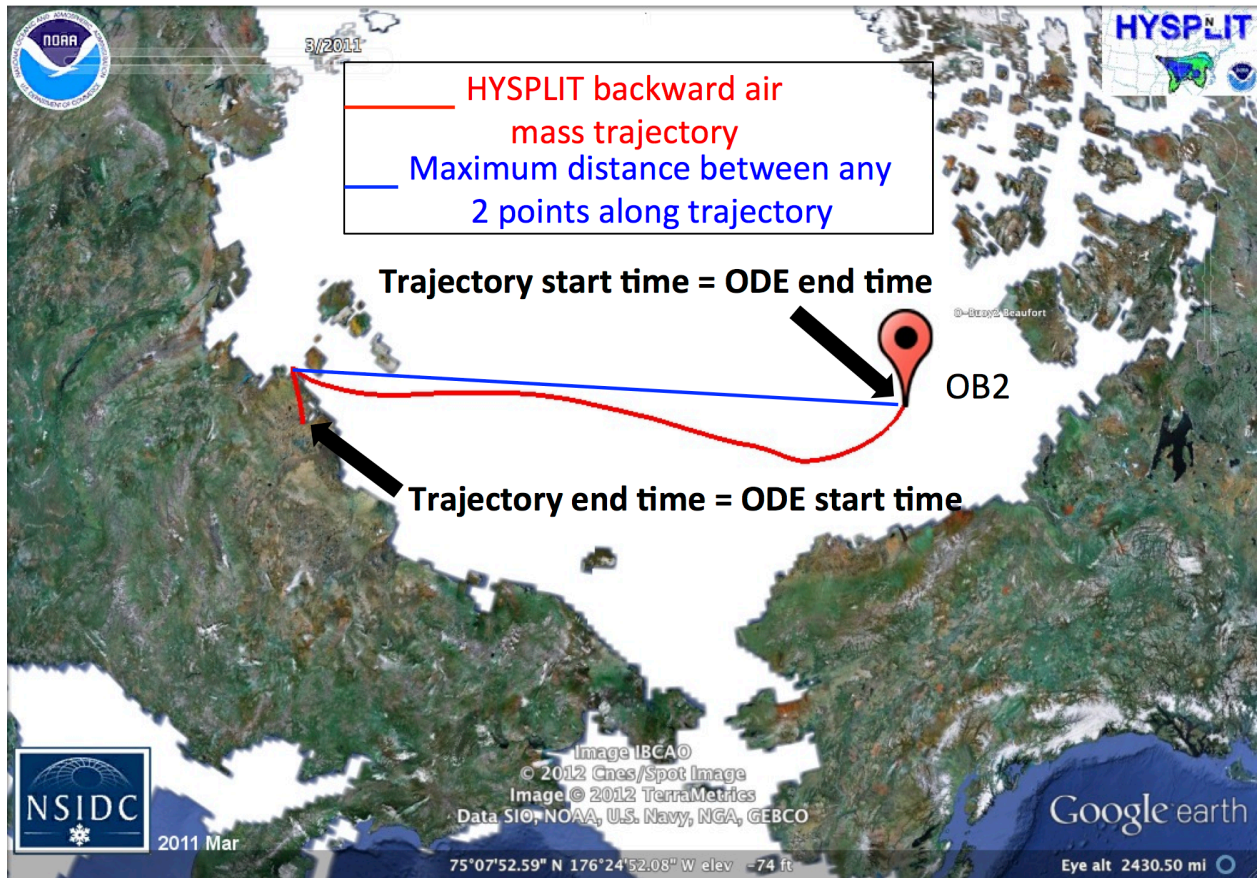
1080   Figure 4: Example HYSPLIT backward air mass trajectory. The HYSPLIT model was run

1081   backward starting from the ODE end time until the ODE start time. ODE spatial dimensions

1082   were determined by calculating the maximum Great Circle distance between any two points

1083   along the trajectory.
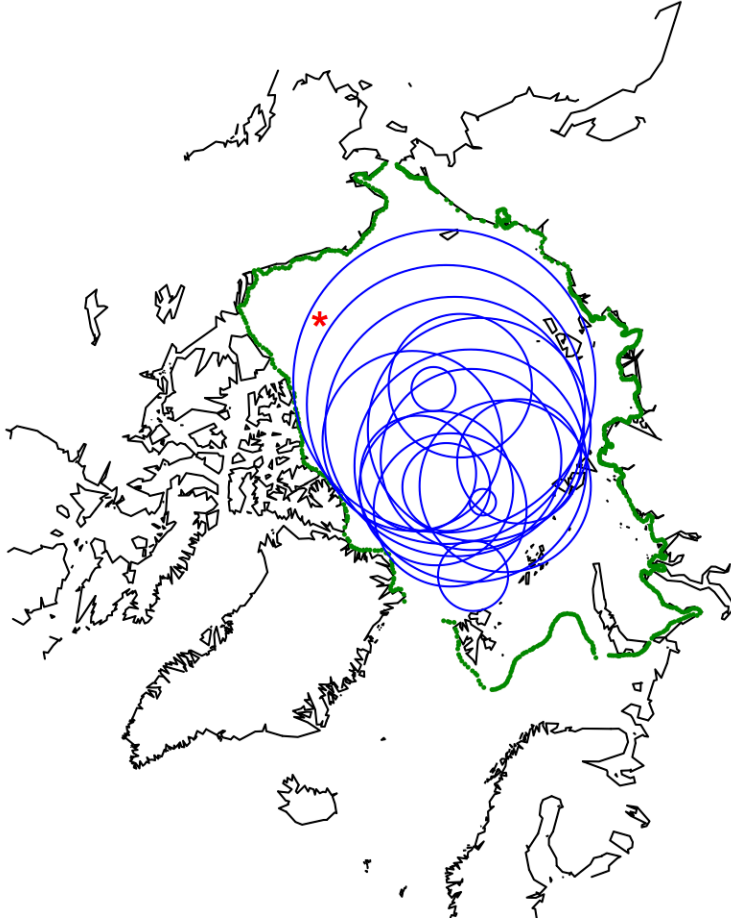
Figure 5: Visualization of one iteration out of 2000 of the Monte Carlo experiments. The area of interest within the Arctic is defined by the green outline. Blue circles represent ODE air masses. The red star represents the average location of the O-Buoy between O-Buoys1 and 2. Seventeen different sized air masses were randomly placed simultaneously within the area of interest.
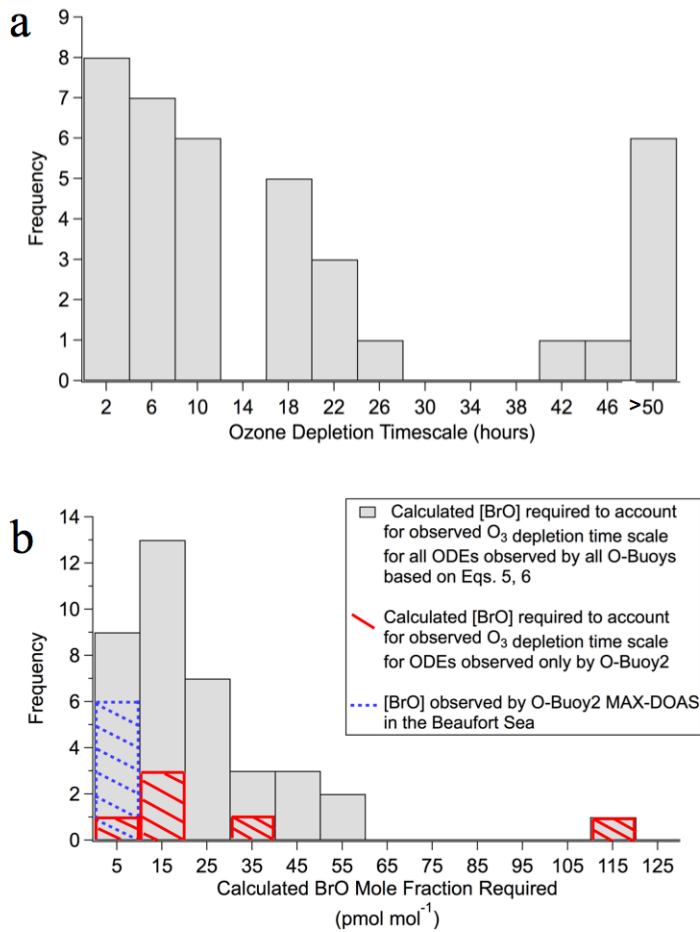
Figure 6: a) Histogram of the distribution of calculated O_3 depletion timescales during ODEs. To more clearly show the majority of events, the six events with τ_{O_3} greater than 50 hours are grouped together on the histogram. b) Calculated BrO concentrations are shown for the observed ODEs, assuming local chemistry, considering BrO and an assumed ClO mole fraction of 6 pmol mol^{-1}, and other O_3 destruction pathways, using Eq. 6 as discussed in Sect. 3.1. The mode calculated BrO mole fraction is 15 pmol mol^{-1}. Measured BrO for O-Buoy2 is shown as the blue hatched bar, and the corresponding BrO required to account for the observed ozone depletion rates for O-Buoy2 events are shown as solid red diagonal bars.
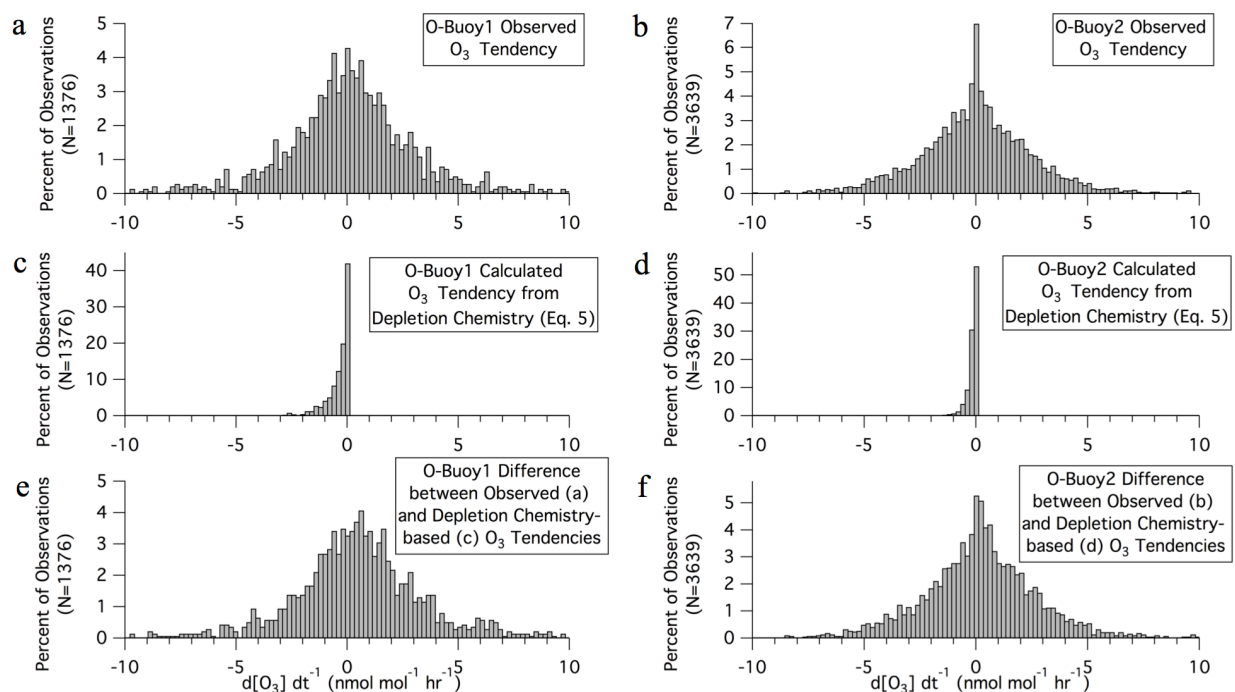
1099

1100 Figure 7: Histogram of the O_3 tendency for observations from O-Buoy1 at Barrow, AK (a,c,e),

1101 and O-Buoy2 in the Beaufort Sea (b,d,f). Top plots (a, b) show the distributions of observed O_3

1102 tendencies between consecutive BrO measurement points. Middle plots (c, d) represent the O_3

1103 tendency distribution based on the depletion chemistry accounted for by Eq. 5. Bottom plots (e,

1104 f) result from the difference of the observed O_3 tendency (a, b) and the contributions of the

1105 chemistry accounted for by Eq. 5 (c, d).

a)

ODEs

Mean: ~1013 km
Median: 877 km
Mode: ~891 km

b)

MODEs

Mean: ~472 km
Median: 282 km
Mode: ~89 km
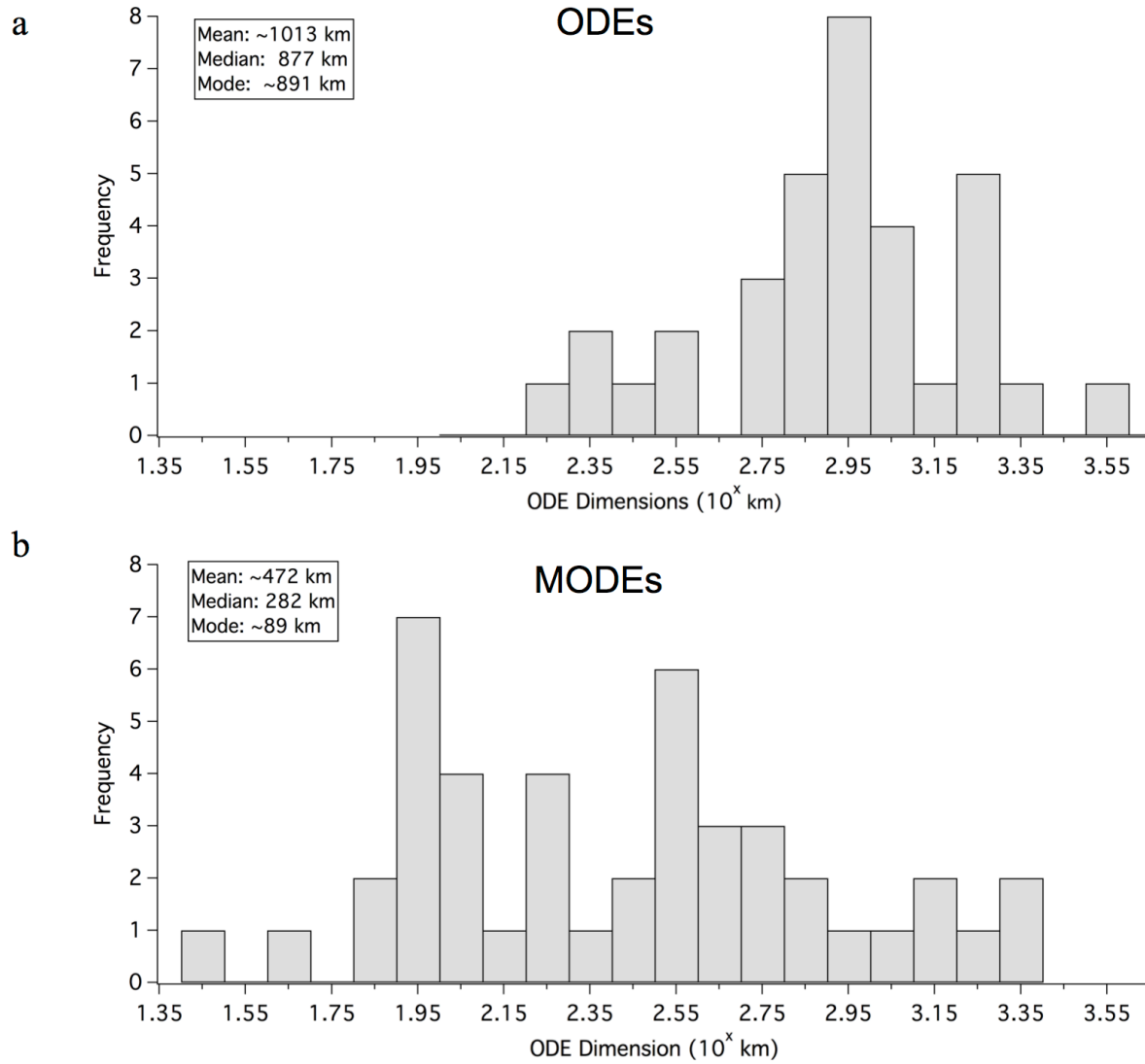
1106

1107   Figure 8: a) Histogram of ODE dimensions for all ODEs. The median of the distribution is 877

1108   km. b) Histogram of dimensions of MODEs. The median of the distribution is 282 km.

1109

1110

Figure 9: Results from Monte Carlo simulation experiment. a) Based on the size distribution as defined by the ODE definition ($O_3 \leq 15$ pmol mol^{-1}), circular areas were shown to not overlap with the site of the O-Buoy 58% of the time (mode = 0), followed by an overlap of one circle 33% of the time. b) Plot of the probability that an individual circle overlaps with the measurement site vs the size of the circle.
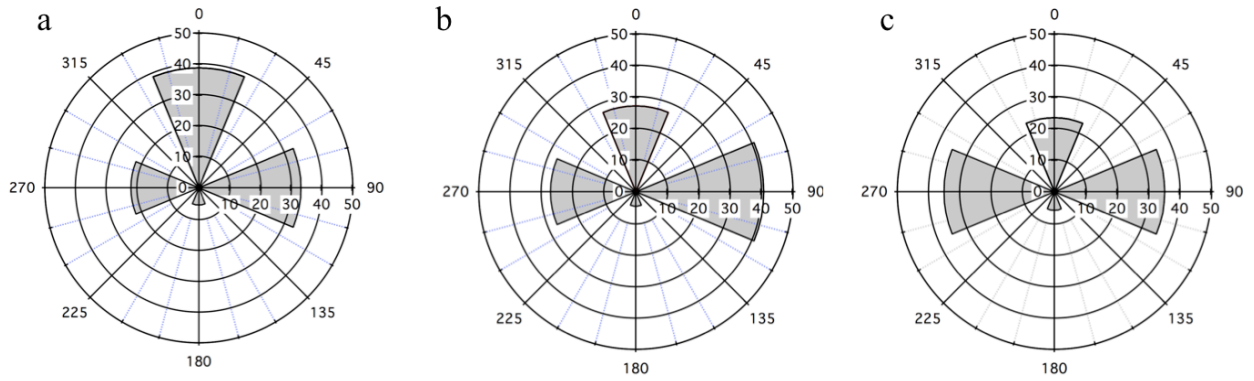
1111

1112

1113

1114

1115

1116

1117
1118
1119
1120
1121
1122
1123
1124
1125

Figure 10: Wind rose plots based on the HYSPLIT backward air mass trajectories showing measured wind direction (degrees) and frequency (%), for a) ODEs, b) MODEs, and c) non-ODEs observed during the two O-Buoy Beaufort Sea deployments (see Fig. 1; Table 1).
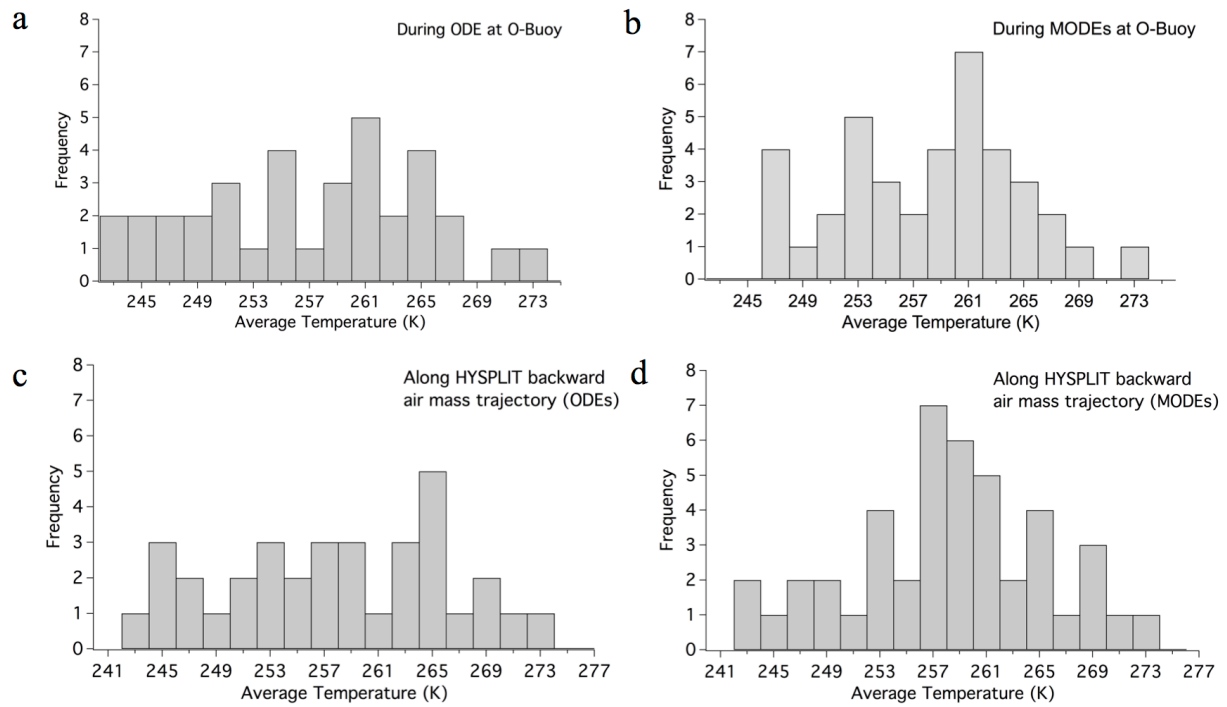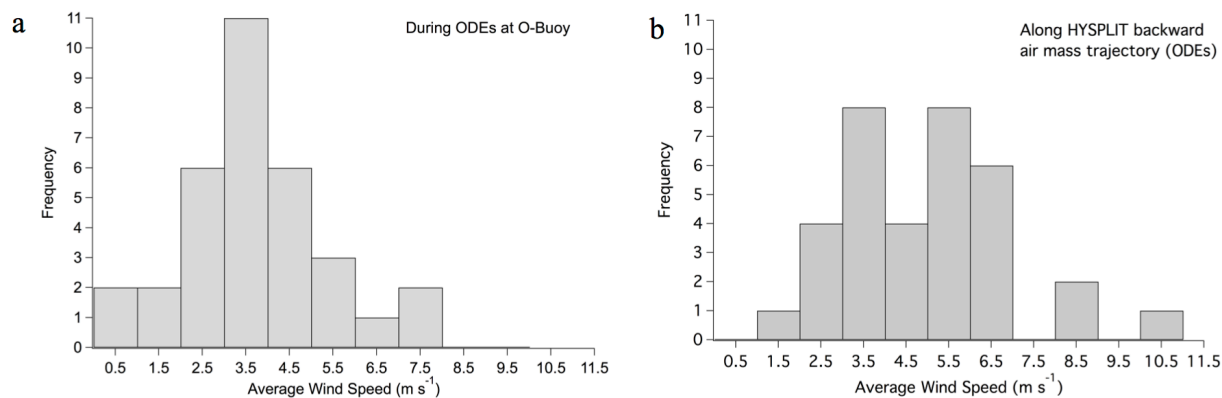
Figure 11: Histograms of the average ambient temperature measured by the O-Buoys during a)
ODEs and b) MODEs. Histograms of the average temperature along the HYSPLIT backward air
mass trajectories for c) ODEs and d) MODEs.

1140

1141   Figure 12: a) Histogram of the average wind speed measured by the O-Buoys during ODEs. b)

1142   Histogram of average wind speeds from O_3-depleted air masses, as determined from the

1143   HYSPLIT backward air mass trajectories.

1144

1145